④

RADC-TR-87-209
Final Technical Report
November 1987

AD-A189 623

CONFORMAL MICROSTRIP SLOT ANTENNA AND ANTENNA ARRAY

University of Pennsylvania

Moshe Kisliuk, Bernard Steinberg and William Whistler

DTIC
ELECTE
JAN 05 1988
S
H
D

ROME AIR DEVELOPMENT CENTER
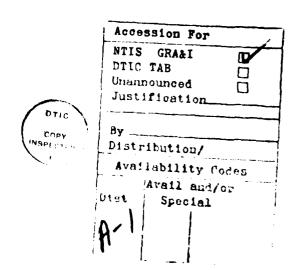Air Force Systems Command
Griffiss Air Force Base, NY 13441-5700

REPORT DOCUMENTATION PAGE

Form Approved
OMB No. 0704-0188

1a. REPORT SECURITY CLASSIFICATION UNCLASSIFIED	1b. RESTRICTIVE MARKINGS N/A
2a. SECURITY CLASSIFICATION AUTHORITY N/A	3. DISTRIBUTION/AVAILABILITY OF REPORT Approved for public release;
2b. DECLASSIFICATION/DOWNGRADING SCHEDULE N/A	distribution unlimited.
4. PERFORMING ORGANIZATION REPORT NUMBER(S) N/A	5. MONITORING ORGANIZATION REPORT NUMBER(S) RADC-TR-87-209

6a. NAME OF PERFORMING ORGANIZATION University of Pennsylvania	6b. OFFICE SYMBOL (If applicable)	7a. NAME OF MONITORING ORGANIZATION Rome Air Development Center (EEAA)
6c. ADDRESS (City, State, and ZIP Code) Valley Forge Research Center Moore School of Electrical Engineering Philadelphia PA 19104		7b. ADDRESS (City, State, and ZIP Code) Hanscom AFB MA 01731-5000

8a. NAME OF FUNDING/SPONSORING ORGANIZATION Rome Air Development Center	8b. OFFICE SYMBOL (If applicable) EEAA	9. PROCUREMENT INSTRUMENT IDENTIFICATION NUMBER F19628-84-K-0021

8c. ADDRESS (City, State, and ZIP Code) Hanscom AFB MA 01731-5000	10. SOURCE OF FUNDING NUMBERS			
	PROGRAM ELEMENT NO. 61102F	PROJECT NO. 2305	TASK NO. J3	WORK UNIT ACCESSION NO. 47

11. TITLE (Include Security Classification)
CONFORMAL MICROSTRIP SLOT ANTENNA AND ANTENNA ARRAY

12. PERSONAL AUTHOR(S)
Moshe Kisliuk, Bernard Steinberg, William Whistler

13a. TYPE OF REPORT Final	13b. TIME COVERED FROM Dec 83 TO Sep 87	14. DATE OF REPORT (Year, Month, Day) November 1987	15. PAGE COUNT 106

16. SUPPLEMENTARY NOTATION
N/A

17.	COSATI CODES		18. SUBJECT TERMS (Continue on reverse if necessary and identify by block number)
FIELD	GROUP	SUB-GROUP	Microslot Antennae, AWACS, Airborne Arrays,
09	03		Conformal Antennae, Radio Camera, Airborne Sensors,
17	09		Conformal Arrays, Beamforming

19. ABSTRACT (Continue on reverse if necessary and identify by block number)

This final report covers the investigation of two microstrip antenna types, the microstrip slot radiator and the microstrip dual folded dipole. The slot dipole is a wide bandwidth (20%), low efficiency (20%) radiator suitable for use in serial slot arrays, and is subject to beam steering with frequency. Array tests showed 20 dB sidelobes, and methods of varying slot susceptance are discussed. The dual folded dipole (DFD) is a 10% bandwidth designed on dual dielectric substrates; the lower substrate can be a high-K dielectric useful for MMIC front-end designs. A noncontacting coupling is made to the DFD radiator. Tests show a tested gain of +7.3 dBi.

20. DISTRIBUTION/AVAILABILITY OF ABSTRACT ☐ UNCLASSIFIED/UNLIMITED ☒ SAME AS RPT ☐ DTIC USERS	21. ABSTRACT SECURITY CLASSIFICATION UNCLASSIFIED
22a. NAME OF RESPONSIBLE INDIVIDUAL Zachary O. White	22b. TELEPHONE (Include Area Code) (617) 377-2055	22c. OFFICE SYMBOL RADC (EEAA)

DD Form 1473, JUN 86   Previous editions are obsolete.

PREFACE

The Valley Forge Research Center initiated this research to formulate theory and to develop microstrip antennae having radiating nonresonant slots in the upper conductor. Preliminary calculations indicated that such antennae can operate in a wider frequency band than the conventional patch microstrip antennae. Our original work to obtain high angular resolution microwave imaging led to the design of the Radio Camera. Implementation of the Radio Camera led to techniques for beamforming an array which is composed of randomly spaced elements, each element moving in a random fashion. The results of our experiments led us to believe that we could design a conformal microstrip slot antenna. The overall goal of this research effort is to develop an antenna element that may be flush-mounted in the outer skin of the aircraft and placed in an arbitrary location. These elements would be connected to a solid state RF located on the interior surface of the airframe by an electrical feedthrough.

This final report covers the investigation of two microstrip antenna types, the microstrip slot radiator and the microstrip dual folded dipole. The slot dipole is a wide bandwidth (20%), low efficiency (20%) radiator suitable for use in serial slot arrays, and is subject to beam steering with frequency. Array tests showed 20 dB sidelobes, and methods of varying slot susceptance are discussed. The dual folded dipole (DFD) is a 10% bandwidth designed on dual dielectric substrates; the lower substrate can be a high-K dielectric useful for MMIC front-end designs. A non-contacting coupling is made to the DFD radiator. Tests show a tested gain of + 7.3 dBi and a 10% bandwidth under 2:1.

Accession For

NTIS GRA&I	☑	
DTIC TAB	☐	
Unannounced	☐	
Justification		

By _____

Distribution/

Availability Codes

Dist	Avail and/or Special
A-1	

DTIC COPY INSPECTED

SUMMARY

The objective of this three year study has been to develop an antenna element suitable for use in conformal arrays. Conformal arrays are useful for placement on any flat or curved surface, offering low wind resistance and elimination of mechanically scanned antennas on aircraft.

A microstrip transmission system was chosen for this conformal antenna study because of its potential low cost per element; large numbers of antenna can be fabricated simultaneously on large sheets with photolithographic precision.

Two microstrip antenna types were analyzed and reduced to practical designs in this study. The microstrip slot antenna was suggested and analyzed by Dr. Kisliuk and its analysis and performance are detailed in Section 1. Its antenna efficiency of 20% limits it to use in serial arrays. The microstrip dual folded dipole (DFD) was developed at VFRC to provide a higher efficiency radiator that could function as an individual element or as part of electronically steerable phased arrays.

The microstrip slot exhibits wide (40%) impedance bandwidth with demonstrated antenna bandwidths of at least 10% frequency spread to - 3 dB gain points. Its low (20%) efficiency is an inherent property of the slot radiator. Three methods of varying efficiency for producing low sidelobe arrays were investigated and are described. Attempts at raising slot efficiency were made and succeeded at the cost of reducing bandwidth to less than 1%. A conclusion of Section 1 is that the low efficiency slot radiator is only useful in serial arrays which have the undesirable feature of beam steering with frequency.

The microstrip dual folded dipole (DFD) exhibited a high gain of + 7.3 dBi and a moderate bandwidth of 6% under 2:1 VSWR, with an analytically demonstrated increase to 10%. The design is adaptable to use with MMIC front end modules by making one of its two dielectric layers of GaAs. Noncontacting coupling to the DFD is provided by transformer coupling, a desirable feature in millimeter wave phased arrays. A conclusion of Section 2 is that the

- 3 -

microstrip DFD is a viable design for use in millimeter wave arrays employing MMIC receiving, phasing or amplifying functions.

The microstrip DFD is considered a significant hardware development with many potential uses. Further analysis exploiting the high-ϵ substrate and low ϵ superstrate will extend the DFD's utility to currently conceived millimeter wave designs. An experimental design study of the DFD as a phased array element would also aid in comparatively testing this design with other candidates for use in millimeter wave conformal phased arrays.

TABLE OF CONTENTS

TABLE OF CONTENTS

SECTION 2.   THE MICROSTRIP FOLDED DIPOLE AS A PHASED ARRAY ELEMENT

LIST OF FIGURES - SECTION 2 (Pages 84-97)

MICROSTRIP SLOT RADIATOR

1.1 ABSTRACT

This final report covers the investigation of two microstrip antenna types, the microstrip slot radiator and the microstrip dual folded dipole. The slot dipole is a wide bandwidth (20%), low efficiency (20%) radiator suitable for use in serial slot arrays, and is subject to beam steering with frequency. Array tests showed 20 dB sidelobes, and methods of varying slot susceptance are discussed. The dual folded dipole (DFD) is a 10% bandwidth designed on dual dielectric substrates; the lower substrate can be a high-K dielectric useful for MMIC front-end designs. A non-contacting coupling is made to the DFD radiator. Tests show a tested gain of + 7.3 dBi and a 10% bandwidth under 2:1.

1.2 INTRODUCTION

The use of microstrip radiators for large planar arrays has been investigated for many years since microstrip offers low cost methods of fabrication for large planar surfaces using the precision photo etching process. The most successful microstrip radiators to date have drawbacks: the microstrip patch, useful for thin substrates has low (4-5% typical) bandwidth, while the microstrip dipole is most useful on thicker substrates which can support surface waves which produce total internal energy reflection at scan angles within the desired scan volume of planar array designs.

The microstrip slot radiator is an alternative radiator which is studied in this contract. The slot radiator, e.g., as a slot cut in a waveguide wall, is fully characterized in references [1,2], and is known to be comparable in bandwidth to a dipole radiator when matched to its natural input impedance. It was proposed as a microstrip radiator when this transmission line medium became popular in the early 1950's [3]. More recently, work published by Solbach [4] in 1982 described a microstrip slotradiator having the form shown in figure 1.

Solbach viewed the input impedance of the microstrip slot radiator as being two quarter-wave stubs in shunt, their internal gap producing a radiating slot one-half wavelength in length. Maximum bandwidth is achieved when the stub impedance - impedance of lines framing the slot - is twice the transmission line impedance. The two stubs in shunt thus provide an input impedance matching the transmission line, and provide a good match and good slot excitation over a reasonable bandwidth. In particular, when the total path length from input to output of one "stub arm" equals 180°, a perfect match is obtained at that frequency. Solbach does not consider any coupling across the radiating slot in his analysis.

In Section 1.3, Dr. Moshe Kisliuk, one of this study's investigators, notes that the lines framing the slot of figure 1 can be considered as two coupled lines excited in antiphase at the lines' centerpoint. The two coupled lines are shorted and roughly one-quarter wavelength long. The properties of microstrip coupled lines are described in the literature [5,6]; the antiphase voltage excitation strongly couples to the odd mode of the coupled line system. The shorted quarter-wavelength coupled system has this input impedance:

$$Zin = ZoTan\beta_{odd}\ell$$

The coupled line system shunting the transmission line will provide a zero reflection when $\tan(\beta_{odd}\ell)$ equals infinity or $\beta_{odd}\ell$ equals 90°. Because the odd mode phase velocity differs from the microstrip line shade velocity, this characteristic provides a second point of zero reflection coefficient. The combination of two zero-reflection points produces a wider frequency bandwidth with low input reflection. This is the impact of Prof. Kisliuk's microstrip slot analysis as described in section 1.3 of this study.

The microstrip slot radiator has a low radiation efficiency, roughly 20% power radiated at X band, or -7 dB in gain relative to a dipole radiator. This

magnitude is of the same order as radiation from an edge-fed coax-to-microstrip transistion detailed in [7], and early measurements at VFRC detailed in section 1.5 were corrupted by combination with the transition radiation. Best results reported in section 1.5 were obtained with a coaxial transition combined with a shorted quarter-wave section which reduced feed radiation by -7 dB to a level that mainly contributed beam tilt to the resultant patterns.

The low antenna efficiency limits the use of the microstrip slot radiation to series slot arrays. Such arrays have limited utility because the main beam changes beam angle, or "steers", with frequency. Kisliuk did a limited amount of array work at Tel Aviv University which is reported in section 1.4.

Section 1.6 reports on attempts to raise the microslot's efficiency to approach 100%. The most successful methods involved capacity coupling to the framed microstrip slot. The radiator produced a high-gain, narrow (.5% typical) bandwidth radiator. It was evident that the shorted-stub equivalent circuit did not apply. Efforts to raise the bandwidth by changing line impedance and configuration produced no significant bandwidth change.

Section 1.7, the conclusion is made that the microstrip slot radiator is a low efficiency radiator suitable only for serial arrays. Arrays of ten or more slots can raise the antenna efficiency above 80% to produce a radiator of useful efficiency level, but this serial array has the undesirable characteristic of beam steering with frequency. As a result of these studies, technical effort on this program was redirected in September 1986 toward producing a high efficiency medium bandwidth element, preferably one capable of circular polarization. Section 2 describes the results of this study.

1.3 SLOT IMPEDANCE ANALYSIS

1.31 GENERAL COMPONENT DESCRIPTION

The microstrip slot being studied on this current contract consists of a single radiator whose slot is excited by the interrupted microstrip current. Since it is a single radiator, it does not possess the frequency sensitivity of the patch antenna it is intended to replace but only that of the slot itself, which has a large frequency bandwidth. Tested microstrip-fed slot circuits have exhibited 40% input impedance bandwidth under 1.5 VSWR and greater than 10% gain bandwidth within 3 dB points.

1.32 THE EQUIVALENT CIRCUIT OF A MICROSTRIP-FED RADIATING SLOT

The upper view of a microstrip-fed slot antenna is shown in Figure 1.1. The microstrips on both sides of the slot are parallel coupled microstrip lines, where the odd mode voltage generates a voltage distribution across the slot [8]-[10]. The equivalent circuit of the upper half of the slot is shown in figure 2. V_1, I_1 and V_2, I_2 are the voltages and currents in the coupled microstrips.

At the reference planes T-T (see Figures 1.1 and 1.2) the coupled microstrips are connected through two right-angle bends at the upper end of the slot (for symmetric bends, i.e., W1 = W) is shown in Figure 1.3 [11].

The Transition for the input and output feeding 50-ohm microstrip lines to the coupled microstrips enveloping the slot are microstrip T-junctions [12], [13]. The equivalent circuit of a T-junction is shown in Figure 1.4 [13], and the equivalent parameters are found in [13] or [10]. From Figures 1.1 and 1.2 it follows that both arms of the T-junctions are symmetrically loaded by the upper and lower parts of the slot, and the equivalent circuit of each of the junctions can be reduced to the circuit shown in Figure 1.5.

1.33 THE INPUT IMPEDANCE OF A SINGLE MICROSTRIP-FED SLOT ANTENNA

The voltage and current in each of the coupled microstrips shown in Figure 2 are linear combinations of even and odd mode traveling waves. The characteristic admittances and the complex propagation constants of the even and odd modes are, respectively,

$$Y_e \text{ and } \gamma_e = a_e + j\beta_e, \tag{1.1a}$$

$$Y_o \text{ and } \gamma_o = a_o + j\beta_o. \tag{1.1b}$$

The even mode does not generate any voltage across the slot, hence the attenuation constant a_e and accounts only for the intrinsic losses of the even mode.

The odd mode generates a voltage across the slot, and

$$a_o = a_r + a_i \tag{1.2}$$

where a_r accounts for the radiation losses of the odd mode, while a_i adds the intrinsic losses of the odd mode.

The values of Y_e, Y_o, and β_o were found by utilizing the design equation of [14].

The input impedance of the coupled microstrips shown in Figure 1.2 is

$$2Z_{in}^o = \frac{V_{in}^o}{0.5\ I_{in}^o} = -\frac{V_1(d/2)}{I_1(d/2)}, \tag{1.3}$$

and

$$2Z_L^O = \frac{V_L^O}{0.5\ I_L^O} = -\frac{V_2(d/2)}{I_2(d/2)} \qquad (1.4)$$

is the load impedance at the output terminals of the coupled lines shown in Figure 1.2.

Straightforward procedures lead to the following expression for the input impedance of the coupled microstrips enveloping the slot [8], [9]:

$$Z_{in}^O = 0.5\ \frac{S(W_1 + W_2\tanh\theta_e) - U_i\tanh\theta_o - U_2}{Y_e S(W_2 + W_1\tanh\theta_e) - Y_o(U_1 + U_2\tanh\theta_o)} \qquad (1.5)$$

where

$$\theta_e = \Upsilon_e d/2, \quad \theta_o = \Upsilon_o d/2 \qquad (1.6a)$$

$$S = -\frac{(U_1 + 2U_2 Y_o Z_L^O)\tanh\theta_o + 2U_1 Y_o Z_L^O + U_2}{(W_2 + 2W_1 Y_e Z_i^O)\tanh\theta_e + 2W_2 Y_e Z_L^O + W_1} \qquad (1.6b)$$

$$W_1 = \frac{2}{1 - \dfrac{A_{21}}{Y_e A_{11}}}, \quad W_2 = W_1 - 2\ , \qquad (1.6c)$$

$$U_1 = \frac{2}{1 - Y_o A_{12}/A_{11}}\ , \quad U_2 = U_1 - 2. \qquad (1.6d)$$

The A parameters in (1.6c) and (1.6d) are the matrix elements of a single right angle bend, as shown in Figure 2.

$$A_{11} = 1 - \omega^2 LC, \quad A_{21} = j\omega C, \quad A_{12} = j\omega 1\ (2-\omega^2 LC)$$

If the width of the microstrips forming the meander line (Figure 1.2) is less than the thickness h of the dielectric, it is recommended to neglect the influence of the right angle bends (Figure 1.3) at the ends of the slot, and to reduce the T-junctions (Figure 1.5) at the transitions from the straight microstrips to the meander line to simple connections, as in Figure 1.6. This recommendation is based on the results of laboratory measurements. The implementation of the above requires the following assumptions:

$$A_{11} = 1, \ A_{12} = A_{21} = 0, \ A_{11}^T = 1, \ A_{12}^T = 0,$$

Z_{in}^O at port BB in Figure 5 = Z_{in} at Port CC in Figure 1.5.

The load impedance seen at the output (reference plane) of the meander line (Figure 1.6) correlates the output voltage with the output current.

$$Z_L^O = Z_L = \frac{V_L}{I_L} = \frac{V_2 \ (\xi = d/2)}{2I_2 \ (\xi = d/2)} \ , \ \text{or}$$

$$2Z_L = \frac{V_e \cosh\theta_e - V_o \sinh\theta_o}{-Y_e V_e \sinh\theta_e + Y_o V_o \cosh\theta_o} \ , \tag{1.7}$$

where

$$\theta_e = Y_e d/2, \ \theta_o = Y_o d/2. \tag{1.8}$$

The even and odd mode ratio is found from (1.7).

$$V_e = V_o \frac{\cosh\theta_o}{\cosh\theta_e} S, \quad S = \frac{2Y_o Z_L + \tanh\theta_o}{2Y_e Z_L \tanh\theta_e + 1} \tag{1.9}$$

- 15 -

The input impedance of the meander-line radiating slot is

$$Z_{in}^{o} = Z_{in} = \frac{V_1(\xi = d/2)}{-2I_1(\xi = d/2)} \text{, or}$$

$$Z_{in} = 0.5 \frac{S + \tanh\theta_o}{Y_e S\tanh\theta_e + Y_o} \text{.} \qquad (1.10)$$

The reflection coefficient from the input of the meander line is

$$p = \frac{Z_{in} - Z_c}{Z_{in} + Z_c} \text{,} \qquad (1.11)$$

where Z_c is the characteristic impedance of the feeding (straight) microstrip line. The voltage at the input of the meander line is $V_{in} = V_o(S\cosh\theta_o + \sinh\theta_o)$, or (Figure 1.6), $V_{in} = (1 + p)V_{inc}$, where V_{inc} is the voltage of the wave incident upon the input. The voltage of the odd mode is

$$V_o = \frac{1 + p}{S\cosh\theta_o + \sinh\theta_o} V_{inc} \text{.} \qquad (1.12)$$

The voltage at the output of the meander line is

$$V_L = V_o (S\cosh\theta_o - \sinh\theta_o) \text{ or}$$

$$V_L = (1 + p) \frac{S - \tanh\theta_o}{S + \tanh\theta_o} V_{inc} \text{.} \qquad (1.13)$$

The voltage of the wave transmitted beyond the meander line slot radiator is

$$V_t = \frac{V_L}{1 + p_L} \text{ , or}$$

$$V_t = \frac{(1 + p_-) (S - \tanh\theta_o)}{(1 + p_L) (S + \tanh\theta_o)} V_{inc} \text{ ,} \qquad (1.14)$$

where

$$p_L = \frac{Z_L - Z_c}{Z_L + Z_c} \qquad (1.15)$$

is the reflection coefficient at the output of the meander line.

1.34 THE RADIATION EFFICIENCY OF A SINGLE MICROSTRIP-FED SLOT RADIATOR

The above analysis shows that the radiating slot is a lossy two-port. Hence, the radiation efficiency (including the intrinsic losses) is found by measuring the S-parameters.

$$\eta = (1 - |S_{11}|^2 - |S_{12}|^2) \ 100\% \qquad (1.16)$$

The radiation efficiency can also be computed as the ratio of the average power dissipated in the network, due to radiation and intrinsic losses, to the power carried by the incident wave in the feeding microstrip line. Straightforward manipulations yield

$$\eta = 400 \frac{G_{in}^{on} + \left| \frac{V_L^o}{V_{in}^o} \right|^2 G_L^{on}}{M[(1+G_{in}^n)^2 + (B_{in}^n)^2]} \% ,$$ (1.17)

where

$$G_{in} + jB_{in} = \frac{1}{Z_{in}} ,$$ (1.18a)

$$G_{in}^o = Re\left(\frac{1}{Z_{in}^o}\right) ,$$ (1.18b)

$$G_L^o = Re\left(\frac{1}{Z_L^o}\right)$$ (1.18c)

and the superscript n indicates that the admittances are normalized to (i.e., multiplied by) the 50-ohm impedance of the feeding microstrip line; the ratio in the numerator of (1.17),

$$\frac{V_L^o}{V_{in}^o} = \frac{V_2(d/2)}{V_1(d/2)} = \frac{SQ_1 + Q_2}{SQ_1 - Q_2}$$ (1.19)

is found from analysis of coupled microstrips in Section 1.32. Recalling the simplifying assumptions in section 1.32, we note $W_1 = 2$ and $W_2 = \theta$. Thus,

$$Q_1 = W_1 = Z ,$$ (1.20a)

$$Q_2 = W_1 \tanh\theta_o = 2\tanh\theta_o$$ (1.20b)

- 18 -

where S, W_1, W_2, θ_e and θ_o are also determined in the same section. A good approximation for the term M in the denominator of (1.17) is

$$M = 1 \qquad \qquad \text{(1.21)}$$

1.35 THE RADIATION LOSSES OF A MICROSTRIP-FED (DIELECTRIC-BACKED) SLOT ANTENNA

To compute the input impedance and the radiation efficiency of a single slot it is necessary to find the values of a_e and a_o (see (1.1) and (1.2)); a_e and a_o account for the even and odd modes intrinsic losses, and are found in literature (e.g., [12] and [13]). The attenuation constant a_r which is due to radiation has been found by equating the average power radiated by the slot at resonance frequency to the input average power of the equivalent lossy transmission line at resonance. The equivalence follows from equal sinusoidal voltage distributions.

A rigorous method for the computation of the complete power radiated into a half space by a slot cut in an infinite conducting screen, and explicit expressions for the complex power of a slot with a sinusoidal voltage distribution has been obtained by Rhodes [15].

An expression for the average power radiated by a center-fed dielectric backed slot with a sinusoidal voltage distribution $\sin(\beta|x|)$ has been given in [16]. For the quasi-resonant frequency of the slot

$$\beta_o d = \pi, \qquad \qquad \text{(1.22)}$$

the average power radiated by a microstrip-fed slot antenna is

$$P_{rad} = \left|\frac{V_o}{8\pi\eta}\right|^2 \frac{a^2 + 1}{a} T , \qquad \qquad \text{(1.23)}$$

- 19 -

where V_0 is the voltage at the center of the slot, η is the intrinsic impedance of a vacuum ($\sim$377 ohm),

$$a = \sqrt{\varepsilon_{eff}^{odd}} \qquad (1.24)$$

ε_{eff}^{odd} is the effective permittivity of the odd mode in the coupled microstrips (Figure 1.2) of Section 1.32.

$$T = Cin[\pi(1+1/a)] - Cin[\pi(1-1/a)] - \frac{2a}{1+a^2}[1 + \cos(\pi/a)] \qquad (1.25)$$

$$- \pi \frac{a^2 - 1}{a^2 + 1} \{Si[\pi(1+1/a)] - Si[\pi(1-1/a)]\},$$

$$Cin(x) = \int_0^x \frac{1 - \cos t}{t} dt, \qquad (1.26a)$$

$$Si(x) = \int_0^x \frac{\sin t}{t} dt, \qquad (1.26b)$$

The center-fed slot is equivalent to a center-fed lossy transmission line with the odd mode characteristic impedance $2Z_0$ and its complex propagation constant. The input average power of this line at resonance

$$P = |V_0|^2 \frac{\tanh(\alpha_r d/2)}{2Z_0}, \qquad (1.27)$$

accounts for the radiation losses.

Equating (1.23) and (1.27) one obtains an explicit expression for the radiation attenuation constant.

$$\alpha_r = \frac{2}{d} \tanh^{-1} (\frac{a^2 + 1}{a} \frac{Z_o T}{480\pi^2}).$$ (1.28)

In the present study, a_r is considered frequency-independent, and the even mode attenuation constant a_e is neglected ($a_e = o$).

1.36 EFFICIENCY OF N-ELEMENT SLOT ARRAY

Dr. Kisliuk computed these radiation efficiencies by the method of Section 1.34:

Band	Freq., GHz	Measured	Computed
VHF	.765-900	3.5%	6-7%
S-band	2.45-4.05	8.12%	7-13%
X-band	8.25-12.0	20-29%	10-15%

Such low efficiency values make the single slot useless as a transmitting radiator because the remaining energy would typically be inefficiently wasted in a terminating load. However, low efficiency radiators are ideal for series-fed arrays: they can either be used in a nonresonant array (loaded termination) or resonant array (shorted termination). The latter implies that a resonant condition is established along the length of the array, which seriously limits the array bandwidth.

An array of low efficiency antennas serially connected will have an enhanced efficiency, since each element reduces the total energy available for the succeeding element. As an example of this effect, Dr. Kisliuk measured 80% efficiency on his 13-element array. For an array of N elements, an expression for power available to the second element may be derived:

- 21 -

$$P_1 = (1-\mu)P_{IN}$$

Similarly, the power lost in the termination for an N-element array is:

$$P_N = (1-\mu)^N P_{IN}$$

Curves of array efficiency and load power vs. number of elements are shown in Figure 1.7 for a nonresonant series array. The curves show that an efficiency of 80% or more is possible for a single slot efficiency as low as 12% for N greater than 13.

Using the last equation, the individual slot efficiency in Professor Kisliuk's measurement is computed to be 12%.

The single slot efficiency was also independently measured at Valley Forge Research Center and is reported as $|s_{31}|^2$ in Figure 1.8. In the frequency region of 8.8 to 10.0 GHz, slot efficiency was measured as 14% to 16% including microstrip losses.

A nonuniform amplitude distribution is required to achieve a low sidelobe level array. In a series array, this is achieved by adjusting individual slot series resistances.

Solbach, in his article on the "Microstrip-Franklin Antenna," [4] derived an expression for series resistance R_S as a function of slotwidth and wavelength. The expression derived assumed uniform coupling across the part of the slot opposite the input and output microstrip lines. Using this assumption, Solbach derived an expression for R_S vs. slot width.

Kisliuk's work has replaced the uniform slot field assumption with one that considers the coupling across the slot in both the microstrip region and the stub regions. This refined analytic approach is expected to result in an improved approximation for R_S and hence improved prediction of low sidelobe array antenna performance because of more accurate amplitude coefficient prediction.

1.4 RADIATION OF MICROSTRIP MEANDER-LINE SLOT ANTENNA

It was observed in [14] that the electromagnetic radiation of microstrip meander-line slot antennas is generated by the voltage distribution of the slot (magnetic current), and by the fractional currents flowing on the upper surface of the straight microstrips feeding the meander line (see Figure 1.6). Hybrid surface waves excited on both sides of the feeding microstrips [16] generate radiation (space) waves at the input and output truncations of the microstrip dielectric board $(z = z_1)$ and $(z = z_2)$; radiation generated by surface waves at the truncation of the dielectric board has also been reported in [16].

This section presents a detailed derivation of the radiation-zone electric fields generated by the slot, by the spillover currents, and by the hybrid surface waves at the truncations of the dielectric board on which the slot antenna has been etched.

1.41 FIELDS IN A SPHERICAL COORDINATE SYSTEM

The computation of the field components in the radiation (far-field) zone requires the introduction of spherical coordinates with the polar axis in the x direction, as shown in Figure 1.10; the Cartesian coordinates in Figure 1.10 are the same as in Figure 1.9. The transition from Cartesian unit vectors to the spherical ones are given by the following formulas:

$$\hat{x} = \hat{r}\cos\theta - \hat{\theta}\sin\theta. \tag{1.29a}$$

$$\hat{y} = \hat{r}\sin\theta\cos\phi + \hat{\theta}\cos\theta\cos\phi - \hat{\phi}\sin\phi, \tag{1.29b}$$

$$\hat{z} = \hat{r}\sin\theta\sin\phi + \hat{\theta}\cos\theta\sin\phi + \hat{\phi}\cos\phi. \tag{1.29c}$$

In the region above the microstrip where $y>0$, the range of the polar angle θ is from 0 to π, and the range of the azimuthal angle ϕ is from $-\pi/2$ to $\pi/2$. For large distances between observation and source point coordinates, the vector potential functions generated by electric and magnetic currents are [17]:

$$\bar{A} = \frac{\mu_o \exp(-jkr)}{4\pi r} \int_V \bar{J}_e \exp(j\psi) dx_o dy_o dz_o, \tag{1.30}$$

$$\bar{A}^* = \frac{\varepsilon_o \exp(-jkr)}{4\pi r} \int_V \bar{J}_m \exp(j\psi) dx_o dy_o dz_o, \tag{1.31}$$

where

$$\psi = \beta_1 x_o + \beta_2 z_o + \beta_3 y_o, \tag{1.32a}$$

$$\beta_1 = k\cos\theta, \tag{1.32b}$$

$$\beta_2 = k\sin\theta\sin\phi, \tag{1.32c}$$

$$\beta_3 = k\sin\theta\cos\phi \tag{1.32d}$$

The angular components of the potential functions (5) and (6) are obtained from (3.1)

$$A_\theta = - A_x \sin\theta + A_y \cos\theta\cos\phi + A_z \cos\theta\sin\phi, \qquad (1.33a)$$

$$A_\phi = - A_y \sin\phi + A_z \cos\phi \qquad (1.33b)$$

The angular (transverse) components of the electric field in the far field (radiation) zone are obtained by utilizing the basic equation for the vector potential functions:

$$\overline{E} = - \frac{1}{\varepsilon_0} \nabla \times \overline{A}^* - j\omega\overline{A} - \nabla\Phi,$$

where Φ is the scalar potential function. In the far-field zone $(\nabla\Phi)_{tr} = 0$, and

$$\nabla \times \overline{A}^* = - \hat{\theta} \frac{\partial A_\theta^*}{\partial r} + \hat{\phi} \frac{\partial A_\theta^*}{\partial r} = jk(\hat{\theta}A_\phi^* - \hat{\phi}A_\theta^*).$$

Thus we obtain explicit expressions for the transverse components of the electric field in the radiation zone:

$$E_\phi = jk(\frac{1}{\varepsilon_0} A_\theta^* - \frac{\eta}{\mu_0} A_\phi), \qquad (1.34a)$$

$$E_\theta = jk(- \frac{1}{\varepsilon_0} A_\phi^* - \frac{\eta}{\mu_0} A_\theta), \qquad (1.34b)$$

- 25 -

1.42 RADIATION FROM THE SLOT

The voltage across the slot is

$$V_{slot} = 2V_o,$$ (1.35)

where V_o is the voltage of the odd mode in the meander line enveloping the slot [4].

It has been shown in Section 1.33 that if the width of the meander line is less than the thickness of the dielectric board, the influence of the right-angle bends at the ends of the slot, as well as the influence of the T-junctions at the input and output of the slot radiator, can be neglected. Simplified expressions for such a meander-line radiating slot are:

$$V_{slot} = V_s \frac{\sinh[\gamma_o(d/2 - |x|)]}{\sinh(\gamma_o d/2)} ,$$ (1.36)

where

$$V_s = 2V_{inc} \frac{1 + p}{1 + S/\tanh(\gamma_o d/2)}$$ (1.37)

is the voltage at the center of the slot, V_{inc} is the voltage wave incident upon the input (Figure 1.2) of the meander line, and p is the reflection coefficient from the input of the meander line radiating slot (Figure 1.1). Explicit expressions for S and p are:

$$V_e = V_o \frac{\cosh\theta_o}{\cosh\theta_e} S, \qquad p = \frac{Z_{in} - Z_c}{Z_{in} + Z_c}, \qquad S = \frac{2\gamma_o Z_L + \tanh\theta_o}{2\gamma_e Z_L \tanh\theta_e + 1} .$$

The equivalent magnetic current density of the slot is

$$\overline{J}_m = -\hat{x} \, 2 \, \frac{V_{slot}}{s} \, \delta(y) \tag{1.38}$$

where s is the width of the slot, and the factor 2 accounts for the influence of the conductive plane surrounding the slot. The substitution of (1.38) into (1.31) yields

$$\overline{A}^* = -\hat{x} \, \frac{\varepsilon_0}{2\pi} \, V_s D \, \frac{\exp(-jkr)}{r} \tag{1.39}$$

where

$$D = \frac{1}{s} \int_{-s/2}^{s/2} \exp(j\beta_2 z)dz \int_{-d/2}^{d/2} \frac{\sinh[\gamma_0(d/2 - |x|)]}{\sinh(\gamma_0 d/2)} \exp(j\beta_1 x)dx. \tag{1.40}$$

The integrals in (1.40) are readily obtained:

$$D = \frac{2\gamma_0[\cos j(\gamma_0 d/2) - \cos(\beta_1 d/2)]}{(\gamma_0^2 + \beta_1^2) \sinh(\gamma_0 d/2)} \, \mathrm{sinc}(\beta_2 s/2), \tag{1.41}$$

where

$$\mathrm{sinc}(x) = \frac{\sin x}{x} . \tag{1.42}$$

The angular components of the vector potential function (1.39) are found (8):

$$A_\theta^* = \frac{\varepsilon_o}{2\pi} V_S D \sin\theta \frac{\exp(-jkr)}{r} ,$$ (1.43a)

$$A_\phi^* = 0.$$ (1.43b)

Equations (1.34) and (1.43) yield the angular (transverse) components of the electric field generated by the slot in the far field zone:

$$E_\phi^{slot} = j \frac{k}{2\pi} V_s D \sin\theta \frac{\exp(-jkr)}{r} ,$$ (1.44a)

$$E_\theta^{slot} = 0.$$ (1.44b)

1.43 RADIATION FROM SPILLOVER CURRENTS

The fractional currents that flow on top of the microstrips [18] are called spillover currents. The back currents flow on the ground plane in the region $|x| > w/2$ (Figure 1.9) and can be replaced by an image strip, carrying the same spillover current in the opposite direction, and placed at a distance 2h from the real strip; it is assumed that the space between the real strip and the image strip ($0 \leq y \leq 2h$) is filled with the dielectric material of the dielectric board.

If the distribution of the spillover currents across the top of the microstrip (x-direction, Figure 1.9) is assumed uniform, the current density vector of the spillover currents is given by

$$\overline{J}_e = \hat{z} \frac{I_s(z)}{w} [\delta(y) - \delta(y + 2h)],$$ (1.45)

where

$$I_s(z) = qI(z)$$ (1.46)

is the spillover current, $I(z)$ is the total current of the microstrip line, and q is a constant [6].

The current distribution on the straight microstrip lines feeding the meander-line slot radiator is found from the equivalent circuit shown in Figure 1.6.

$$I(z) = \begin{cases} \dfrac{V_{inc}}{Z_c} [\exp(-j\beta z) - p\exp(j\beta z)] & \text{for } z_1 \leq z \leq 0 \\[2mm] \dfrac{V_t}{Z_c} [\exp(-j\beta z) - p_L\exp(j\beta z)] & \text{for } 0 \leq z \leq z_2 \end{cases}$$ (1.47)

where V_{inc} is the voltage wave incident on the reference plane $z = -0$, p is the reflection coefficient at $z = -0$, V_t is the transmitted voltage wave at the output of the meander line slot radiator ($z = +0$), and p_L is the reflection coefficient of the "load" at the output terminals of the slot radiators (Figure 1.6); Z_c is the characteristic impedance of the feeding microstrip lines.

The substitution of (1.45), (1.46) and (1.47) into (1.30) yields

$$\bar{A} = \hat{z} \frac{\mu_o}{2\pi} q \frac{V_{inc}}{Z_c} C \frac{\exp(-jkr)}{r}$$ (1.48)

where

$$C = jR\sin(\beta_4 h)\text{sinc}(\beta_1 w/2)\exp(-j\beta_3 h), \qquad (1.49)$$

$$\beta_4 = \sqrt{\epsilon_r}\,\beta_3, \qquad (1.50)$$

$$R = R_1 + R_2 + R_3 + R_4, $$

$$R_1 = \frac{1-\exp[jz_2(\beta_2 - \beta)]-1}{j(\beta_2 - \beta)}, \qquad (1.51a)$$

$$R_2 = -p\,\frac{1-\exp[jz_1(\beta_2 + \beta)]-1}{j(\beta_2 - \beta)}, \qquad (1.51b)$$

$$R_3 = \frac{V_L}{V_{inc}(1 + p_L)}\;\frac{\exp[jz_2(\beta_2 + \beta)]-1}{j(\beta_2 - \beta)}, \qquad (1.51c)$$

$$R_4 = -p_L\,\frac{V_L}{V_{inc}(1 + p_L)}\;\frac{\exp[jz_2(\beta_2 + \beta)]-1}{j(\beta_2 - \beta)}, \qquad (1.51d)$$

V_L is the output voltage of the meander-line slot radiator (see Figure 1.9).

The angular components of the potential function and of the radiation fields generated by the spillover currents are:

$$A_\theta = qV_{inc}\,\frac{\mu_0}{2\pi Z_c}\,C\cos\theta\sin\phi\,\frac{\exp(-jkr)}{r}, \qquad (1.52a)$$

$$A_\theta = qV_{inc}\,\frac{\mu_0}{2\pi Z_c}\,C\cos\phi\,\frac{\exp(-jkr)}{r}, \qquad (1.52b)$$

- 30 -

$$E_\phi^{curr} = - jV_{inc}qk \frac{\eta}{2\pi Z_c} C\cos\phi \frac{\exp(-jkr)}{r} , \tag{1.53}$$

$$E_\theta^{curr} = - jV_{inc}qk \frac{\eta}{2\pi Z_c} C\cos\theta\sin\phi \frac{\exp(-jkr)}{r} , \tag{1.54}$$

For a standard 50Ω microstrip line $(Z_c = 50\Omega)$ the impedance ratio in (1.53) and (1.54) is

$$\frac{\eta}{2\pi Z_c} = \frac{120\pi}{100\pi} = 1.2 \tag{1.55}$$

1.44 RADIATION FROM THE HYBRID SURFACE WAVE AT THE TRUNCATIONS OF THE DIELECTRIC

The microstrip quasi-TEM mode in a microstrip line generates a hybrid surface wave [16] that propagates along the microstrip with the phase velocity of the microstrip mode. It has been shown that the truncations of the dielectric are sources of radiation generated by a surface wave. The electric and magnetic fields of the hybrid surface wave that are tangential to the truncation planes $z = z_1$ and $z = z_2$ (Figure 1.9) are:

$$\bar{E} = \hat{x}E_x + \hat{y}E_y, \tag{1.56a}$$

$$\bar{H} = \hat{x}H_x + \hat{y}H_y, \tag{1.56b}$$

On the input truncation plane $z = z_1$, the outward unit normal is $\hat{n}_1 = - \hat{z}_1$, hence the equivalent current densities are:

$$\bar{J}_{e1} = (\hat{x}H_{y1} - \hat{y}H_{x1})\delta(z-z_1), \tag{1.57}$$

$$\bar{J}_{m1} = (-\hat{x}E_{y1} - \hat{y}E_{x1})\delta(z-z_1), \tag{1.58}$$

On the output truncation plane $z = z_2$, the outward unit normal is $\hat{n}_2 = -\hat{z}_2$, and the equivalent current densities are:

$$\bar{J}_{e2} = (\hat{x}H_{y2} - \hat{y}H_{x2})\delta(z-z_2), \tag{1.59}$$

$$\bar{J}_{m2} = (-\hat{x}E_{y2} - \hat{y}E_{x2})\delta(z-z_2), \tag{1.60}$$

It has been shown that the field components of a hybrid surface wave are:

$$E_x = \begin{cases} E_{xi}f_3 & \text{for } y \le h \\ E_{xe}f_4 & \text{for } y \ge h \end{cases} \tag{1.61a}$$

$$E_y = \begin{cases} E_{yi}f_1 & \text{for } y \le h \\ E_{ye}f_2 & \text{for } y \le h \end{cases} \tag{1.61b}$$

$$H_x = \begin{cases} H_{xi}f_1/\eta & \text{for } y \le h \\ H_{xe}f_2/\eta & \text{for } y \ge h \end{cases} \tag{1.61c}$$

$$H_y = \begin{cases} H_{yi}f_3/\eta & \text{for } y \le h \\ H_{ye}f_4/\eta & \text{for } y \ge h \end{cases} \tag{1.61d}$$

The functions f_i in (1.61 are:

$$f_1 = sV\cos(\xi y\_\exp(-\alpha_x v + j\beta z), \tag{1.62a}$$

- 32 -

$$f_2 = sVexp(-\alpha_x v - \alpha_y u + j\beta z), \tag{1.62b}$$

$$f_3 = sVsgn(x)sin(\xi y\_exp(-\alpha_x v + j\beta z), \tag{1.62c}$$

$$f_4 = sVsgn(x)exp(-\alpha_x v - \alpha_y u + j\beta z), \tag{1.62d}$$

$$u = y - h, \tag{1.63}$$

$$v = \begin{cases} x-w/2 & \text{for } x > w/2 \\ -x-w/2 & \text{for } x < -w/2 \end{cases} \tag{1.64}$$

$$sgn(x) = \begin{cases} 1 & \text{for } x > w/2 \\ -1 & \text{for } x < -w/2 \end{cases}. \tag{1.65}$$

V is the voltage of the microstrip quasi-TEM lmode, and s is the excitation constant, which for a Duroid 5880 ($\varepsilon_r = 2.2$) 50Ω line is 0.01.

The substitution of (1.59)-(1.65) into the integrands of (1.30) and (1.31) yields

$$\overline{A} = \frac{\mu_o}{\eta} V_{inc} \frac{s}{4\pi} Q_5 (\hat{x}Q_1 + \hat{y}Q_2) \frac{exp(-jkr)}{r}, \tag{1.66}$$

$$\overline{A}^* = \varepsilon_o V_{inc} \frac{s}{4\pi} Q_6 (\hat{x}Q_3 + \hat{y}Q_4) \frac{exp(-jkr)}{r}, \tag{1.67}$$

- 33 -

where $Q_1 - Q_6$ are:

$$Q_1 = - (H_{yi}P_4 + H_{ye}P_6)P_2, \qquad Q_2 = (H_{xi}P_3 + H_{xe}P_5)P_1,$$

$$Q_3 = (E_{yi}P_3 + E_{ye}P_5)P_1, \qquad Q_4 = - (E_{xi}P_4 + E_{xe}P_6)P_2,$$

$$Q_5 = Q_7 - Q_8, \qquad Q_6 = Q_7 + Q_8.$$

The image components of the electric and magnetic currents in the region $y < 0$ due to the conductive ground plane (which is assumed infinite) are analytical continuations of the functincs (1.62a) and (1.62c); the "cosine" components have an even image, while the "sine" components have an odd image. Thus, the hybrid wave radiation is generated mostly the the E_y and H_x components of the hybrid wave.

The transverse components of the radiation field generated by the hybrid surface wave due to the truncation of the dielectric are:

$$E_\phi^{hybr} = jV_{inc} \, s\frac{k}{4\pi} \, [Q_6(Q_4\cos\theta\cos\phi - Q_3\sin\theta) + Q_2Q_5\sin\phi] \, \frac{exp(-jkr)}{r} \quad (1.68)$$

$$E_\theta^{hybr} = jV_{inc} \, s\frac{k}{4\pi} \, [Q_5(Q_1\sin\theta - Q_2\cos\theta\cos\phi) + Q_4Q_6\sin\phi] \, \frac{exp(-jkr)}{r} \quad (1.69)$$

1.45 TOTAL RADIATION FIELD

The total radiation field is the sum of the fields derived above.

$$E_\phi = E_\phi^{slot} + E_\phi^{curr} + E_\phi^{hybr}, \qquad (1.70)$$

$$E_\theta = E_\theta^{curr} + E_\theta^{hybr}. \qquad (1.71)$$

The radial component of the pointing vector is

$$\pi = (|E_\phi|^2 + |E_\theta|^2)/(240\pi), \qquad (1.72)$$

and the total power radiated by the microstrip slot antenna which is

$$P_{rad} = \int_{-\pi/2}^{\pi/2} d\phi \int_0^\pi d\theta r^2 \pi \sin\theta \qquad (1.73)$$

can be found by numerical calculations.

1.5 EXPERIMENTAL RESULTS - TEL AVIV UNIVERSITY

1.51 IMPEDANCE TESTS

Figures 1.11 - 1.14 show the measured and computed frequency dependence of the input VSWR of single microstrip-fed slot antennas connected at the output to matched loads; the VSWR of the X-band slot in Figure 1.13 has been calculated in a simplified way, neglecting the influence of the T-junctions and of the right angle bends at the end of the slot. The calculations of the VSWR of the X-band slot in Figure 1.14 were not performed because of computer shortcomings at Tel-Aviv University.

The discrepancy between the computed and measured radiation efficiency of the X-band slot is seemingly due to the additional radiation ascribed to the spillover currents.

The presented study shows that microstrip-fed slot antennas and slot arrays are operational in wider frequency bands than conventional microstrip patch antennas, and microstrip slot arrays require less space for the same number of elements.

- 35 -

1.52 TAPERED MEANDER LINE SLOT ARRAY INVESTIGATIONS

An array of 13 slots is shown in Figure 1.15; the width of slots is tapered leading to a taper in the amplitude of the voltage at the center of the slots. The widths of the slots are:

$$s_1 = s_{13} = 0.374 \text{ mm} \qquad s_2 = s_{12} = 0.282 \text{ mm}$$

$$s_3 = s_{11} = 0.189 \text{ mm} \qquad s_4 = s_{10} = 0.141 \text{ mm}$$

$$s_5 = s_9 = 0.116 \text{ mm} \qquad s_6 = s_8 = 0.104 \text{ mm}$$

$$s_7 = 0.100 \text{ mm}$$

The radiation patterns of that array (Figure 1.15) are shown on Figure 1.16; the sidelobe level is about - 15 dB.

Another array of 10 slots, where the width w of the straight microstrip lines feeding the slots is tapered, is shown in Figure 1.17. The design of this array is based on the relationship [4]:

$$R_s \Omega = 45 \left(\frac{\lambda_o}{w} \right)^2 .$$

The radiation patterns of the 10-slot array in Figure 1.17 are shown in Figure 1.18; the sidelobe level is lower than -15 dB. The measured radiation efficiency of these arrays is above 75%.

1.6 EXPERIMENTAL STUDIES - VFRC

1.61 HIGH EFFICIENCY MICROSLOT STUDY

It is evident that a high efficiency slot would be more universally useful than the low efficiency slot, since the latter can only achieve useful efficiencies (> 80%) by the formation of a series slot array. An antenna element with broad beam pattern in two orthogonal planes is more desirable for wide angle two dimensional arrays, so a study of methods of terminating a line with a microstrip slot was initiated.

A method of matching by capacity coupling has been found and is described. An antenna study has been conducted which shows the microstrip slot radiator exhibiting an increase in gain as the slot area is increased. Currents in the metal surrounding the slot excite nonradiating hybrid modes in the dielectric, which radiate at the edges of the dielectric. When compared to the microstrip patch radiator, the microslot radiator's pattern is broader and gain is lower. Its bandwidth in this mode appears lower than the patch radiator's for the same dielectric thickness.

1.61a DETERMINATION OF MATCHING TECHNIQUE

To begin the study, experiments were made to find a suitable matching network for a radiator termination a 50-line microstrip line. A matching study following the microstrip was investigated and rejected, after trials of a series of stub lengths of various impedance produced no indication of matching potential. Attempts at matching by varying the input line impedance to present different impedance levels to the microslot also produced only high input reflection conditions.

A successful matching system was finally obtained by capacity coupling to the transverse microstrip line containing the slot, treating this last as a resonant circuit. This system could always be made to match by adjusting

capacity by varying coupling slot width. The resulting configuration is shown in Figure 1.19.

A useful measurement parameter is the cavity Q of this resonant circuit. For any shunt resonant circuit, cavity resonance is indicated by zero reactance, or a normalized impedance of $1 + j0$. The reciprocal of the frequency difference between the $\pm$ 45 degree phase conditions or between normalized impedances of $1 \pm j1$ is defined as the cavity Q. VSWR at the level $1 \pm j1$ impedance levels is 2.6:1: this level is similar to the 2:1 and 3:1 bandwidths common in discussing microstrip patches and other radiators, and is convenient for comparing this radiator with others.

Resonant frequency of the shunt microslot radiator is directly related to the total patch length of the 100 ohm metal line surrounding the microstrip slot using the effective dielectric constant calculated for the 100 ohm line. Typical cavity Q's for the radiators measured here varied between .6% and .76% for a .031" (.787 mm) thick substrate. Resonant frequencies varied from 8 GHz to 9.6 GHz for various configurations; for a representative frequency of 9 GHz, this thickness is .024 λ.

1.61b EFFECT OF FEEDING SYSTEM ON ANTENNA PATTERNS

The need for improving the feed system to reduce feed effects on pattern was noted in Interim Reports. The pattern in Figure 1.20 is typical of the edge feeding system. The beam peak of the shunt-fed microslot radiator shows a beam tilt of 48°, indicating the influence of direct radiation from the coaxial feed at board edge.

The pattern improvement obtained by using the rear feed with entry point through the ground plane is clearly shown in Figure 1.21. This pattern shows a more uniform pattern with the beam tilt reduced to 15°. The beam tilt remaining is believed to be caused by radiation from the coaxial feedline or the .33 λo long 50 ohm microstrip feedline.

The rear feed approach has been adopted in all succeeding testing because of its clear reduction of interference from direct radiation with the micros-lot radiator patterns.

1.61c EFFECTS OF SLOT AREA ON ANTENNA GAIN

The microslot as a shunt radiator acts like a slot antenna in a ground plane with respect to antenna gain, having a low radiation efficiency because of low physical area. To investigate the effect of radiator area on gain, the three substrates shown in Figure 1.22 were fabricated.

The .2 mm microslot's antenna pattern is shown in Figure 1.23. The ap-pearance of shoulders on the main lobe pattern is believed due to radiation from the dielectric truncations at $\pm$ 1.78 cm from the center of the microslot (the substrate edges). They are most prominent in this low-gain microslot because they are similar in magnitude to the direct microslot radiation. The extraneous radiation at + 90° and at 180° angles cannot be caused by the microslot because its pattern factor approaches zero for end-fire direction. End fire radiation thus must be caused by radiation of hybrid mode energy from the truncated dielectric edges of the substrate.

The .5 mm shunt microslot antenna pattern of Figure 1.24 shows con-siderable reduction of shoulders from dielectric edge radiation, probably because of the 2.3 dB increase in gain for this radiator.

The gain increase with the wider slot prompted the design of the "vee-slot" radiator which was hand-fabricated because of time pressures. The resulting pattern shown in Figure 1.25 exhibits a 4.2 dB gain increase over the .5 mm microslot pattern. This is a significant gain improvement and is the shunt microstrip slot radiator form most closely competitive with the microstrip patch radiator.

1.61d COMPARISON OF SHUNT MICROSTRIP SLOT AND MICROSTRIP PATCH RADIATORS

A comparison of the microstrip vee-slot and patch radiators is given below:

COMPARISON OF PATCH AND VEE-SLOT RADIATORS

	Vee-Slot Microslot	Microstrip Patch*
Gain	+ 5 dB measured	+ 6.7 dBd Calculated
Bandwidth	.64% measured for	2.4% Calculated for
2:1 VSWR	t/λ_o = .035	t/λ_o = .035

* Source: Reference [12]

Most significant is that the vee-slot antenna measured gain approaches that of the calculated microstrip patch gain.

Bandwidth for VSWR = 2:1 indicates superior performance for the patch antenna. These are directions indicated for improving vee-slot bandwidth, the principal one being to use a lower impedance line to surround the microstrip slot. However, it appears impossible for the vee-slot bandwidth to approach the patch bandwidth.

The capacity coupling method used in feeding the vee slot is difficult to control tolerances on if edge coupling of microstrip lines is the capacity mechanism. Any other capacity mechanism, such as soldered-on chip capacitors, nullifies the microstrip advantage of being a low cost fabrication process.

To summarize, the vee-slot antenna appears to be the microstrip slot implementation that is the closest competitor for the microstrip patch antenna. Its lower bandwidth and tolerance-sensitive coupling mechanism make it inferior to the patch for similar applications in its present form.

1.62 SERIES SLOT INVESTIGATION

The series microstrip slot as originally conceived by Prof. Kisliuk continues to be the main thrust of this contract's effort. Efforts were made to improve pattern measurement techniques and to broaden our understanding of the microstrip slot antenna.

A pattern study of a series slot radiator is detailed, with patterns taken in a test fixture that minimizes the pattern interference of the dielectric truncation radiation.

1.62a MATCH IMPROVEMENT TECHNIQUES

An impedance study of the rear-mounted connector was made using two rear-mounted connectors mounted on a 13.72 cm (5.4") 50-ohm line. The connector matching time cycle was shortened by the discovery that a tapered resistive card laid on top of the microstrip offered more than 10 dB insertion loss and thus isolated reflections from the distant connector from those of the input port connector by attenuation. This system allowed studying connector impedance by modifying only the input connector dimensions.

A connector having a .085" teflon diameter was chosen because the .093" wide 50-ohm line will block radiation from the feedlines. The original .010" diameter center conductor introduced a fixed series inductance: this was minimized by increasing the center conductor diameter to .027".

The final connector configuration is shown in Figure 1.26. The resulting single connector VSWR was under 1.1 VSWR from 8.0 to 11.0 GHz. This design is duplicated in all test fixtures used in this report period.

Mitering slot ends and microstrip line ends at each connector made small reductions in VSWR and thse changes were incorporated. The resulting impedance performance of a .2 mm x 12.1 mm slot on a 5.4" run is shown in Figure 1.27:

the VFRC test data compare favorably with the Tel-Aviv University data also illustrated.

1.62b DIELECTRIC LAYER TRUNCATION EFFECTS

Dielectric-coated conductors, as noted in [7] and discussed in Section 1.44, can support a nonradiating hybrid mode which radiates at a dielectric truncation. Figure 1.28 shows an example of this effect: the radiation pattern of a single .2 mm slot in the center of a 15.25 cm board having both metal ground plane and dielectric sheet ending at $\pm$ 7.63 cm from the slot. The multilobed pattern results from the reradiation at the board ends which are 4.32 wavelengths apart at 8.5 GHz, the test frequency.

In Figure 1.28, there are two predominant cyclic pattern systems - one having a 22° period and the other a 14° period. The separation of pattern nulls should be related to $\sin^{-1}\lambda/L$, where L is the separation of radiators in the two-radiator system.

It is interesting to try the spillover radiation hypothesis of Section 1.4 on this system, considering L as 2.16 λ, half the board length, and assuming the 50-ohm line velocity of 1.37 times free space velocity. Then

$$\Delta\phi = 1.37 \ (2.16\lambda) \sin 22° = 399°.$$

Since $\Delta\phi$ is by definition 360°, a velocity error of $(1-399/360) = 10.9\%$ is indicated by the computation. To force the 360° result, a reduction of $\sqrt{-}_e$ from 1.37 to 1.236 is required. Thus, a spillover current-generated hybrid mode with a velocity 10.9% lower than the 50 ohm microstrip velocity is indicated.

Testing then continued on the 35.6 x 50.8 mm board with the .5 mm x 12.6 mm shunt slot sketched in Figure 1.19. The slot radiation pattern shown dotted

- 42 -

in Figure 1.29 has a theoretical slot's beamwidth of 55°, but shows deviations at the -15 dB level, indicating the possible presence of radiation from dielectric truncations.

The solid trace is the same radiator set in a 38 cm long by 20 m wide ground plane: the metal edges are now spaced 38 cm while the dielectric sheet width remains at 3.56 cm. The metal sheet edge effects are clearly indicated by a fine ripple relating to the 10.8-wavelength separation of the metal edges. The overall pattern distortion remains present in the radiation pattern, however, indicating the probability of dielectric truncation radiation effects.

Two possible sources of excitation of hybrid modes are apparent:

- the spillover currents carried on the top of the 50 ohm feedlines as discussed in Section 1.4.
- radiation from the microstrip open circuit at the junction of the microstrip-to-coaxial line adapter.

As described above, it is possible that spillover currents on the 6.85 cm feedlines are significant radiation sources in the 15.25 cm board pattern shown in Figure 1.27. On the short runs of the 3.56 cm board patterns shown in Figure 1.28, however, it is possible that the microstrip open circuit of the microstrip-coax adapter is the major contribution to hybrid mode excitation/dielectric truncation radiation. This possibility is also discussed in connection with the serial slot patterns of the next section.

1.62c SERIES SLOT PATTERN

One goal of this study has been to determine the microslot antenna's useful bandwidth as a radiator. The final unit tested shown in Figure 1.26 was most free from extraneous radiation effects and was measured over the 8.0 to

11.0 frequency band (Figures 1.31-1.33) to permit that measurement. Its VSWR is given in Figure 1.30.

The vee-slot antenna was also tested because it had achieved higher gain than the slot in the shunt radiator version. It had lower measured gain than the .5 mm slot radiator, which confirmed the validity of Dr. Kisliuk's analysis of the microstrip slot as a coupled line system, a feature not present in the vee-slot design. Its pattern at 9 GHz is shown in Figure 1.34.

Antenna patterns were taken from 8 to 11 GHz; typical patterns for the .5 x 12.6 mm slot are shown in Figures 1.31-1.33 and summarized in the graphs of Figure 1.35. At 8 GHz, the pattern beamwidth is slightly greater than theoretical (58° vs. 56° theoretical), has good pattern symmetry to a -15 dB level, and shows little beam tilt. The 9 GHz pattern shows a shoulder developing near +90°, a lobe developing at -90° and a change of sign of the beam tilt. In the 10.5 GHz pattern, the energy at -90° has reached -7.5 dB with a definite null appearing at +23° right.

The pattern beam tilt appears related to the substrate board width: at the zero beam tilt frequency of 8.4 GHz seen in Figure 1.35b, the substrate is exactly 1.0 wavelengths wide. The pattern null, however, appears related to radiation from the microstrip open circuit at the input microstrip/coax adapter. Consider that the substrate edge and the microslot act as a 2-radiator set: at 10.5 GHz, computation of path lengths shows that these two sources are 180° out of phase when viewed at -23°, the angle of the pattern null. The fact that this effect occurs only on the input connector side of the pattern indicates that only input connector radiation is involved in distorting the pattern.

1.62d GAIN AND EFFICIENCY

The antenna gains measured in this study are referred to the gain of a half-wave dipole for testing convenience. To relate to the average power

radiated a fictitious isotropic radiator is defined which has uniform radiation over a spherical shell surrounding the antenna. The dipole gain relative to an isotrope is given in various references as 1.64 or +2.15 dB. One should also note that all measured gains include dielectric and I^2R losses in the antenna. Directivity also relates to main beam peak power relative to an isotropic source, but excludes any I^2R or dielectric losses. Directivity, therefore, can be defined analytically without involving the specific antenna material or other considerations.

Efficiency must be defined relative to the theoretical gain or directivity of the antenna type chosen; e.g., the slot radiating into a half space defined by the infinite ground plane containing the slot. The theoretical gain into a half space is +3 dB above the dipole or +5.15 dB above an isotrope. An efficiency scale calculated on this basis is shown in the right-hand ordinate of Figure 1.35's gain slot.

The patterns in the 8.0 - 9.0 GHz region are relatively undistorted by the reradiation from the dielectric truncation as evidenced both by pattern symmetry and absence of endfire lobe at -90°, and the efficiency shown in this region (20-25%) relates closely to the values measured and reported in the First Interim Report, and in Section 1.34 of this report.

The values of gain above 9 GHz are suspect because of distortion from truncation radiation. This increased radiation, it is noted, correlates with the increased input reflection coefficient: it is expected that improved connector match would eliminate the end-fire radiation and improve the gain correlation with the lower frequency readings.

1.63 A VARIABLE EFFICIENCY CONFORMAL ELEMENT

The microstrip slot radiator devised by Dr. Kisliuk under the current RADC contract has exhibited a medium bandwidth (1 to 2 GHZ at X-band) while

exhibiting a low efficiency (15-20%, also in the X-band). Because of this low efficiency, its use in an antenna requires serial arrays of a number of microslots, in order to raise the antenna efficiency to a useful value greater than 80%, which represents a 1 dB power loss in the terminating load.

A nonuniform amplitude distribution is required to achieve a low sidelobe level. In a series array, this is accomplished by adjusting individual slot .efficiencies and thus adjusting a slot's radiating power. Tests reported here demonstrate a way of varying the microslot antenna's efficiency. The mechanism for adjusting the slot efficiency is to place the slot between two equal susceptances so as to form a cavity between them, resonant at or near the slot resonant frequency. Recalling resonant cavity theory, the electric field at cavity center, the slot location, should be Q times the nonresonant line current. The line current that excites the slot is thus increased; hence the slot's radiated power and efficiency are increased.

The antenna patterns of Figures 1.36a and b verify this concept: the single microslot of Figure 1.36a has 1.3 dB lower gain than the microslot between two susceptances of Figure 1.36b.

Antenna efficiency is determined by relating the element gain to an ideal radiator: in this case, it should be a slot radiating into a half space of 2π steradians, which would have a maximum gain of 3 dB above a dipole radiator. Thus the gains of the two elements of -2.2 dB and -3.5 dB below standard dipole gain represent peak values of -5.2 and -6.5 dB below the ideal radiator. Noting that % efficiency = 100 x log (ΔdB/10), we determine the antenna efficiencies as 31.6% and 22.4%, respectively, for the microslot with and without susceptances.

The effect of a second variable, the cavity line impedance, was also studied. The line impedance between susceptances was lowered to 42 ohms by widening the microstrip line, which resulted in an added 0.9 dB gain and a new efficiency value of 37%, as shown in Figure 1.36c.

All three cases exhibit VSWR values (see Figure 1.37) of less than 2:1 over at least a 2 GHz band, which represents a 20% bandwidth for the microslot element. The VSWR value of 2:1 is selected both for comparison to the microstrip patch radiator and because the associated reflection loss of -0.5 dB is considered a practical loss limit for an antenna. Best VSWR performance under 2:1 VSWR over a 3 GHz band is shown by the slot plus two-susceptance radiator with 42-ohm line between susceptances.

This design study leads to the conclusion that the slot radiator between two susceptances is a useful design unit for cascading to form a serial array.

1.7 CONCLUSIONS

The experimental and analytical studies described in this report detail information on two forms of microstrip slot radiator, the shunt form terminating a feedline and the serial form.

The shunt microslot radiator has a dipole pattern and exceeds 60% efficiency. It has a bandwidth determined by the stub line impedance and the substrate thickness and material. Its bandwidth in the present form is .6% and requires improvement before being a useful competititor for the patch antenna. The present microslot design compares unfavorably with the patch radiator in bandwidth.

The serial form of microslot radiator when measured with improved test methods exhibited dipole-like patterns when not distorted by radiation from dielectric truncations, and exhibited 20-25% efficiency. The pattern bandwidth exceeding 1 GHz was shown by patterns. Nonradiating hybrid modes can be generated by the microstrip launcher open circuit stub line as well as by spillover currents on conductors. These modes transform to radiating modes at dielectric edge truncations. Thus radiation's magnitude is strongly correlated with input impedance match.

REFERENCES: SECTION 1

[1] J.O. Kraus, "Antennas", McGraw-Hill, 1950

[2] S. Silver, "Handbook of Antenna Design", McGraw-Hill, 1949, MIT Rad Lab Series, Vol. 12

[3] E.G. Fubini, "Stripline Radiators", IRE Trans. MTT-3, pp. 149-156, March 1955

[4] K. Solbach, "The Microstrip-Franklin Antenna", IEEE Trans. AP-S, Vol. AP-30, pp. 733-735, July 1982

[5] M.K. Krage and G.I. Haddad, "Frequency Development Characteristics of Microstrip Transmission Lines", IEEE Trans. MTT, Vol. MTT-20, pp. 678-688, 1972

[6] T. Bryant and J. Weiss, "Parameters of Microstrip Transmission Lines and Coupled Pairs of Microstrip Lines", IEEE MTT-16 Proc. '68, pp. 1021-1027

[7] J. James, P. Hall and C. Wood, "Microstrip Antenna Theory and Design", Peter Piregrinus Ltd., 1981

[8] M. Kisliuk, "Lossy Transmission Line Model of a Microstrip Slot Antenna", VFRC QPR No. 43, April-Sept. 1983, pp. 76-81

[9] M. Kisliuk, Y. Twaig, and A. Axelrod, "The Input Impedance and Radiation Efficiency of Microstrip Fed Slot Radiators", submitted to AP-S for publication.

[10] Y. Twaig, M.Sc. Thesis, Tel Aviv University, 1984, M. Kisliuk-Advisor (in Hebrew)

[11] M. Kirschning, R.H. Jansen, and N.H.L. Koster, "Measurements and Computer-Aided Modeling of Microstrip Discontinuities by an Improved Resonator Method", 1983 IEEE Intl. Microwave Symp., Boston, pp. 495-497

[12] K.C. Gupta, R. Garg and I.T. Bahl, "Microstrip Lines and Slotlines", AR Tech House, 1979

[13] "Microwave Integrated Circuits", Springer-Verlag, 1984 (in German)

[14] M. Kisliuk and W. Whistler, "Microstrip-Fed Radiating Slots and Slot Arrays", VFRC QPR No. 45, pp. 46-65, April-Sept. 1984

[15] D.R. Rhodes, "On the Stored Energy of a Planar Aperture", IEEE Trans.-AP, Vol. AP-14, pp. 673-683, Nov. 1966

[16] M. Kisliuk and A. Axelrod, "Hybrid Surface Waves in Microstrip Lines", VFRC QPR No. 47, pp. 69-75, April-June 1985

[17] C.A. Balanis, "Antenna Theory: Analysis and Design", Harper and Row, Inc., New York, 1982

[18] L. Lewin and T. Ruehle, "A Note on the Complex Poynting Vector and on the Fraction Current on the Upper Surface of a Microstrip Line", IEEE Trans.-AP, Vol. AP-29, pp. 144-147, 1981

2. THE MICROSTRIP DUAL FOLDED DIPOLE AS A PHASED ARRAY ELEMENT

2.1 ABSTRACT

The microstrip dual folded dipole is described as a candidate for next generation micro and millimeter wave phased array systems. A multilayer, multidielectric microstrip system is used that is compatible both with low cost etch processing of dielectric sheets and with MMIC active device technology using GaAs or silicon substrate as underlayer. A novel transformer coupling is made between feed and radiating layers that avoids metallic interconnections.

A performance analysis of input impedance is presented that employs analog (Smith Chart) derivation of dipole impedance combined with computer modeling of the element and feed system. Theory and experimental results compare favorably both on input impedance and gain and pattern performance. The microstrip folded dipole radiation exhibits 10% bandwidth (under 2.1 VSWR) with suitable input matching; this compares favorably with a predicted 4-5% for the microstrip patch radiator.

2.2 BACKGROUND

Arrays of metallic elements printed on a dielectric sheet are strong candidates for future phased arrays because of the inherent low cost of forming array faces from continuous sheets and the ease of controlling production tolerances through use of the photo-etching processes. The excellent tolerance control of this process will permit extending printed circuit arrays into the millimeter-wave region.

Much technical concern has been concentrated on the combination of monolithic MIC technology with antenna systems for large scale arrays. This combination is most useful at millimeter wavelengths where the available area per element (1.6 x 1.6 mm at 94 GHz for a fully filled array) is a practical

working dimension for current GaAs fabrications. Using a multilayer dielectric system with a GaAs lower substrate allows the phased array designer to implement a variaty of per-element signal processing concepts; the simultaneous use of a low-ϵ superstrate supporting a radiating element permits designing a large phased array system with no surface wave resonances which would produce angles of total energy reflection within the desired scan volume.

In the drive toward the next generation of phased arrays, many workers have concerned themselves with the scanning problems of large dielectric-faced array apertures [1], [2], [3]. In particular, "blind spots" develop at specific scan angles as a function of the dielectric constant, material thickness and frequency. Because the blind spot scan angle is a strong function of these parameters, the use of high dielectric constants is unattractive. This point is well illustrated in Figure 2.1 which compares surface wave propagation constants (onset of surface wave modes). Pozar and Schaubert [2], [4] have compared infinite arrays of printed-circuit dipoles and microstrip patch radiators, and found similar scanning and blind-spot behavior for both radiator types for similar d, ϵ_r and λ values. The printed circuit dipole has attractive impedance characteristics, bandwidth potential and design freedom when the substrate thickness (in wavelength units) approaches 0.25. The scan angle response (Figure 2.2), however, shows a blind spot at an angle near 45°, severely limiting this design's use in large planar arrays. Similarly, the microstrip patch radiator has good scan characteristics at low substrate thickness, but exhibits a small bandwidth (4% under 2:1 VSWR for h/λ = .047) because of its inherently high Q.

The purpose of the present contract is to find a medium bandwidth, high efficiency conformal element suitable for use in millimeter wave phased arrays that may be flush-mounted in the outer skin of an aircraft and placed in arbitrary locations on the surface.

The Valley Forge Research Center has found in the folded dipole radiator a design combining both good scanning performance and medium (5-10%) bandwidth. It employs a multilayer feed system which lends itself to the combination of active elements on monolithic substrates on one layer with an efficient antenna radiator on the combined layers as illustrated in Figure 2.3. This characteristic, along with the simplicity and low cost of photo-etched arrays, make this design useful in large arrays in centimeter and millimeter-wave bands.

An analytic understanding has been obtained of the Dual Folded Dipole (DFD) radiator reported in reference [5]. The radiation resistance of this radiator has been computed through the use of Smith Chart analysis, and an analytical model is proposed composed of cascaded 2-port matrices. This model and the derived values of R_r and phase are to be used as inputs in further optimization of the DFD for various applications. In addition, a summary of DFD characteristics and a comparison with the microstrip patch are included in this report.

2.3 FOLDED DIPOLE IMPEDANCE

G. Dubost has done considerable examination of the folded dipole radiator above a ground plane at lower frequencies [6]. This is an attractive radiator in that its radiation resistance is higher than that of a dipole above a ground plane: he shows that while the radiation resistance R_r of a flat, open-circuited dipole is

$$R_r = 24\pi^4 \left(\frac{h}{\lambda_o}\right)^2 \qquad \text{h = substrate thickness} \qquad (1)$$

for air dielectric, the folded dipole has a value four times as high for equal width fed and folded arms, with this multiplication ratio widely adjustable [7] by varying the arm width ratio. James, Hall and Wood [8] compared

- 51 -

bandwidths of microstrip folded and patch antennas, indicating a 50% to 200% bandwidth improvement for the folded dipole.

The basic analysis of the folded dipole with unequal arm diameters was provided by Uda and Mushiake [9] and was described more fully in Jasik [10] from their work. The expression for a folded dipole's input impedance is:

$$Z_{in} = \frac{2(1+a)^2 Z_r Z_x}{(1+a)^2 Z_r + 2Z_x}$$
(2)

where $(1+a)^2$ is the impedance step-up ratio

Z_x is the characteristic impedance of the two-wire line formed by fed and folded arms (r_1 and r_2 in Figure 2.4a)

Z_d is the impedance of the equivalent dipole

More recently, Lampe [11] has extended earlier work to microstrip folded dipoles through use of conformal mapping transformations to provide a more exact estimate of $(1+a)^2$, the transformation ratio, and ρ_e, the radius of the equivalent dipole.

A complete wideband analysis requires solution of Z_x, which has been solved by several workers [12]. A center-band analysis is possible, however, by noting that

$$Z_x = j Z_o \tan \left(\frac{K_o L}{2}\right)$$
(3)

with Z_o = impedance of the asymmetric two-wire line and that at resonance:

- 52 -

$$Z_x \rightarrow \text{infinity since } 2Z_x \gg (1+a)^2 Z_r,$$

hence,
$$Z_{in} \rightarrow (1+a)^2 Z_r \qquad\qquad (4)$$

so the resonance solution for Z_{in} requires only determination of Z_r and the impedance transformation ratio. This expression clearly shows the basic advantage of the folded dipole: that a wide range of impedance variation is possible with this design. The impedance of a dipole above a ground plane has been solved by DuBost, and is cited above.

The transformation ratio equation used in references [9], [10] and [11] is given below and is plotted in Figure 4.3:

$$T_Z \;=\; 1 + \frac{\cosh^{-1}\left(\dfrac{(a^2-b^2+1)}{2a} \right)}{\cosh^{-1}\left(\dfrac{(a^2+b^2-1)}{2ab} \right)} \qquad\qquad (5)$$

The parameters $a = d/r$ and $b = \dfrac{r_2}{r_1}$ with d, r_1 and r_2 shown are further explained in Figure 2.4a.

The equivalence between flat and round conductors has been solved by Cohn [13] by conformal mapping techniques

$$\frac{r_o}{\omega} \doteq \frac{1}{4}\left[1 + \frac{t}{\pi\omega}\left(1 + \ln\left(\frac{4\pi\omega}{t}\right)\right)\right] \qquad\qquad (6)$$

The approximation $\dfrac{r_o}{\omega} \doteq \dfrac{1}{4}$ is used in [8]. Using this equivalence, new expressions for a and b are derived by substitution:

$$a = \frac{4d}{\omega_1} \quad \text{and} \quad b = \frac{\omega_2}{\omega_1}$$

These terms are explained in Figure 2.4b.

2.4 FOLDED DIPOLE WITH BALUN: EXPERIMENTAL TESTS

Experiments were conducted at the Valley Forge Research Center to determine the potential utility of the folded dipole. A balun from microstrip to 2-wire line was fabricated to excite the folded dipole. A balun shown in Figure 2.4, and E and H plane antenna patterns, Figures 2.5 and 2.6, were measured: the folded dipole had a measured gain of nm 1 dB above an isotropic radiator. The gain reference was a Narda standard gain horn. This antenna gain, measured in the presence of a large reflection loss caused by impedance mismatch at the antenna terminals, must be corrected by adding this reflection loss. The VSWR is related to impedance ratio:

$$R = VSWR = \frac{Z \text{ line}}{Z \text{ folded}} = \frac{100.1 \text{ ohms}}{9.76 \text{ ohms}}$$

Z line was computed by the LINECALC computer program and Z folded calculated by methods of [6]. The reflector loss is $10 \log 4R/(1+R^2) = 4.9$ dB. The corrected folded antenna gain is thus: $G_f = 1 + 4.9 = +5.9$ dBi. This gain figure is of the same order as the folded dipole gain of 6 to 7.5 dBi cited in [13] and the patch antenna gain of 7.3 dBi cited by Bahl and Bhartia in [12]. The antenna bandwidth for 3 dB loss in gain for this model was found to be ± 300 MHz around an 8300 MHz peak gain, or 7.2%.

Experimental emphasis has been shifted by 4:1 scaling from 8.8 GHz to 2.2 GHz, increasing microstrip dimensions by that ratio to simplify fabrication, with emphasis being given to designing an improved balun for better impedance match. A rationale for improving the balun performance is found by noting its

two-part character; first, there is a 180° U-bend that is 180 electrical degrees long at center frequency; second, there is a two-wire line conducting energy in the balanced mode to the folded dipole. A study was therefore undertaken to improve the input impedance match by lowering the connecting two-wire line impedance to approach that of the folded dipole through the use of a quarter-wavelength impedance matching section.

An estimate of the folded dipole impedance is made using the parameters of the S-band model. Polystyrene sheets with ϵ = 2.5 and 0.125" thickness were available; a total substrate thickness of .250" was considered allowable (h/λ = .047 at 2.2 GHz) under the array scanning limitations described in the background section and [1], [2], and [3]. Noting that the apparent dipole height is $\sqrt{\epsilon}$ higher than in air, the microstrip dipole radiation resistance is thus R_R = $24\pi^4 (h\sqrt{\epsilon}/\lambda)^2$ = 12.95 ohms, and for a folded dipole having equal fed and folded arm widths, Z_f = $4R_r$ = 51.78 ohms.

Both the balanced two-wire line impedance and the quarter-wavelength matching section impedance were determined through the use of the "Linecalc" program designed by EESof, Inc. The balanced line impedance is known to be the odd mode of a microstrip coupled line system.

The complete balun was analyzed using EESof's "Touchstone" program. With this program, the entire circuit including coaxial input, a phase-inverting section and quarter-wave matching section were modeled. The program assumes a resistive load at the antenna terminals and does not model the antenna circuit. The circuit of the final balun is shown in Figure 2.7. For this circuit, the impedance after the phase-inverting U-section is 96.4 ohms, and that of the quarter-wave matching section is 52.7 ohms. Predicted transformation output impedance is 28.8 ohms; this shows good agreement with the Touchstone program's computed value of 30 ohms. Predicted balun performance with the 30-ohm termination is shown in Figure 2.8.

Measured performance of an equal-arm folded dipole is also shown in Figure 2.8. The data confirm the ability to match the folded dipole. It exhibits a bandwidth of 50 MHz, or 2.5% under 2:1 VSWR, indicating a need for more accurate impedance modeling of the dipole and the balun circuit. Further study determined that a desirable element for potential use as a circularly polarized radiator should have equal E and H beamwidths. Since the X-band pattern data of Figures 2.5 and 2.6 exhibit a 58° E plane 3 dB beamwidth and a 77° H plane 3 dB beamwidth, an antenna configuration using two dipoles separated in the H plane was designed. Performance of this design is discussed in the next section.

2.5 DUAL FOLDED DIPOLE: IMPEDANCE MODEL

The S-band dual folded antenna developed in the VFRC study is shown in Figure 2.9. There are two microstrip systems used, a microstrip feed line with 3.1 mm spacing and a microstrip dual folded dipole with 6.3 mm spacing. The feed microstrip is embedded in the thicker dielectric of the antenna microstrip, forming a multilayer dielectric system. The radiator is composed of two microstrip folded dipoles at each end of a two-conductor transmission line. The folded dipole's radiation resistance is of the order of four times the microstrip dipole's radiation resistance, and is adjustable by varying the ratio of fed and folded dipole arms as discussed in section 2.3. This system lends itself to current array system thinking incorporating an MMIC RF-IF circuit on one semiconductor substrate and the antenna on a low-ε superstrate.

The transformer coupling between lower layer and two-conductor line eliminates the need for feed-through connections which are difficult and costly to fabricate. Its coupling principle is explained in the voltage diagram of Figure 2.10. There is a reversal of polarity of electric field occurring at the center of the 34.5-ohm half-wavelength cavity in the microstrip transmission line. The electric fields capacitatively couple to the two-wire line on top of the superstrate, exciting this line in its balanced transmission-line mode; the coupled energy travels both ways on the two-wire

line to feed the two folded dipoles. This same feed approach is used by Dubost in his slot microstrip antenna [6]: in that case, an open-circuited stripline excites a slotline feeding two folded dipoles.

Modeling of this structure is simplified by noting that the two radiators and their coupled strip lines from dipole to line center point are in parallel. A new equivalent circuit can be made using the same elements except that the coupled strip line and radiator impedances are replaced by half their values. This change permits the use of the simple cascadable two-part form described in the final analytical model shown in Figure 2.11.

Solving for the folded dipole radiation resistance becomes a matter of determining the transmission line impedance from input to dipole terminals and modeling this system. This is done by transforming from input point to first discontinuity either through manipulation of cascadable transmission line matrices or via the Smith Chart. The process is repeated through each discrete line segment or discontinuity to the antenna terminals.

Figure 2.12 is a Smith Chart showing the antenna input impedance at the connector and the folded dipole input impedance. The bandwidth under 2:1 VSWR is within the scribed 2:1 VSWR circle, and is seen to be roughly 125 MHz or 5.6%. The transformer coupling between antenna and input is seen to be near critical coupling, nearly matched at band center.

The impedances of the microstrip cavity and the coupled strip transmission line are seen to be important variables in achieving a wide bandwidth of input VSWR < 2:1: by adjusting these variables, an overcoupled condition can be produced with an attendant improvement in bandwidth.

The folded dipole impedance data can be used to determine the impedance at the resonant frequency. The impedance at 2220 MHz is 0.96 + $j0$ relative to the 41.78-ohm impedance of the connecting coupled-wire line: in absolute

- 57 -

terms, the antenna impedance is 40.1 ohms. This compares favorably with the 34.2-ohm impedance predicted by the methods outlined in Reference 5:

- microstrip dipole radiation resistance is computed to be 13.18 ohms using Equation (1) of Section 2.3;

- folded dipole multiplication factor $(1+a)^2$ is computed to be 2.59:1 using Equation (5) of Section 2.3;

- the product of these two factors is the theoretical impedance, 34.2 ohms.

The difference between the calculated and measured values could be caused by these and other factors:

. round-off error in the Smith Chart transformations.

. errors in electrical lengths and mechanical dimensions of coaxial transition, transformer and line segments.

. air gaps in board systems and between the 0.05 mm copper foil antenna and polystyrene boards.

Still greater bandwidth improvement can be obtained by adding a transformer in the input circuit to reduce the diameter of the input circular impedance trace while over-coupling. This method has been explored with the Touchstone cascaded matrix program whose two-port component blocks are detailed in Figure 2.11.

The original input circuit detailed in Section 2.3, (i.e., a 50-ohm line to the antenna input terminals at the 34.5-ohm line) was first modeled and compared to the measured input impedance. The resulting impedance trace, shown in Figure 2.13, is seen to be in good agreement with the experimental antenna input trace of Figure 2.12. It was thus possible to explore input impedance improvement options.

The sketch of Figure 2.9 and the Touchstone equivalent circuit of Figure 2.11 detail a matching section added at the antenna input. The improved input impedance trace of Figure 2.14 was achieved by adding a capacitative pad of 34.5-ohm line followed by a length of 60-ohm line as detailed in Figure 2.11.

Figure 2.15 summarizes the bandwidth improvement predicted by the above input circuit change. The initial experimental bandwidth of 5.8% is expected to be increased to 11.4% VSWR under 2:1 as shown in Figures 2.14 and 2.15.

The large predicted bandwidth of the microstrip DFD with input ma⁺ ching is a significant factor in determining the utility of this design for use in millimeter-wave phased-array structures.

2.6 DUAL FOLDED DIPOLE PATTERN CHARACTERISTICS

Figure 2.16 details an antenna system equivalent to the dual folded dipole above a ground plane useful for pattern analysis. The two folded dipole radiators are represented by two dipoles displaced in the +X direction ahead of the ground plane, which lies in the Z plane at X = 0. Two dipoles are displaced in the -X direction: these are images of the first two, and are oppositely phased to fulfill the boundary condition that tangential $\bar{E} = 0$ on the ground plane. The dipole and image pairs analytically describe the pattern in the +X region: the ground plane blocks any energy in the -X region, so no radiation pattern exists there.

The voltage pattern for the four-dipole set can be described [13] by the following formulas, using the geometry shown in Figure 2.14.

$$f(\theta\phi) = \frac{\cos \frac{\pi}{2} \cos\theta}{\sin\theta} \quad \frac{\sin(kh\cos\phi)}{\sin kh} \quad \cos \left(\frac{k_o d}{2} \sin\phi\right)$$

The E plane voltage pattern is in the XZ plane ($\phi = 0$) (Figure 2.17)

- 59 -

$$f_E(\theta) = \frac{\cos\frac{\pi}{2}\cos\theta}{\sin\theta}$$

and the H plane pattern lies in the XY plane ($\theta=90°$) (Figure 2.18)

$$f_H(\phi) = \frac{\sin(kh\cos\phi)}{\sin kh} \quad \cos(\frac{k_o d}{2}) \sin\phi$$

Experimental patterns were also taken at 2.24 GHz at VFRC and are shown dotted on Figures 2.17 and 2.18. There is good agreement between theoretical and measured 3 dB beamwidths in each plane, but the pattern extends beyond ± 90° in each plane because of limited ground plane size.

Cross-polarization performance was measured and is shown in the patterns of Figure 2.19 to be of the order of 18-20 dB in the H Plane and 24-26 dB in the E plane. These low levels could be due to feedline radiation; no investigation of cross-pol energy source was made.

Gain was also measured by comparison to an S-band standard gain horn. The measurement frequency is below the SGH's normal calibration frequency range of 2.6-3.95 GHz; calibration was extended to 2.24 GHz by considering the aperture distribution constant and gain modified only by horn area in wavelengths. In this manner, the horn gain at 2.24 GHz is estimated to be +13 dB above isotropic. Reflection loss from the 1.62:1 VSWR from the waveguide/coaxial adapter adds -0.25 dB, for a horn gain minus R.L. total of +12.75. The dual folded dipole's measured gain under these conditions is + 7.4 dBi.

A comparison is made in Table 1 between the microstrip dual folded dipole and microstrip patch antennas. The two designs are compared for similar dielectrics and thicknesses and designed at the common frequency of 2.24 GHz to rule out effects of these parameters on the comparison. The folded dipole design was described in Section 2.3; the patch design is from a "practical"

design procedure in Reference [14]. Their pattern characteristics are approximated as paired radiators, a dual dipole model being used for the dual folded dipole and a dual slot model used for the patch. These models result in similar beamwidths in the arrayed planes and in the planes of the dipole or slot long dimensions, although they reverse in polarization notation because of the differing radiator characteristics.

The radiators are similar in gain as expected from their similar area: no theoretical DFD gain or measured patch gain information was available. Bandwidth of the DFD is greater than for the patch, 5.5% measured vs. 4% theoretical, although the full bandwidth potential of the DFD has not been realized as yet. Several sources gave conflicting values of patch Q and hence bandwidth, with the values of References [6] and [15] being chosen and in near agreement.

In other characteristics, both radiators share the feature of non-contacting coupling between radiator and a second plane surface containing active receiver/signal processing components, a distinct advantage for millimeter-wave phased-array construction. The DFD offers this feature in a dual layer dielectric configuration above a common ground plane for active and radiating surfaces, while the aperture-coupled patch has active elements below the radiating element's ground plane. The DFD design may make heat-sinking simpler for the active devices, but shares the available area in a fully filled array with the radiating element. Space and heat-sinking considerations would be greatly relieved in a thinned aperture array design.

2.7 CONCLUSIONS

A conclusion can be drawn that the two designs are similar in performance and both are adaptable to millimeter-wave phased-array designs requiring combination with MMIC (monolithic microwave integrated circuit) techniques. The DFD shows a slight bandwidth advantage, an advantage that may improve with more mature DFD designs.

REFERENCES - SECTION 2

[1] R.J. Mailloux, "Phased Array Architecture for Millimeter Wave Active Arrays," AP-S Newsletter, February 1986.

[2] D.M. Pozar and D.H. Schaubert,"Scan Blindness in Infinite Phased Arrays of Printed Dipoles," IEEE TRANS. AP-S, VOL. AP-32, NO. 6, June 1984, pp. 602-610.

[3] R.S. Elliott, "Array Patterns Synthesis, Part II: Planar Arrays," AP-S Newsletter, April 1986.

[4] D.M. Pozar and D.H. Schaubert, "Analysis of an Infinite Array of Rectangular Microstrip Patches with Idealized Probe Feeds," IEEE Trans. AP-S, Vol. AP-32, No. 10, October 1984, pp. 1101-1107.

[5] W.T. Whistler, "The Folded Dipole As A Medium Bandwidth Phased Array Element", Valley Forge Research Center Quality Report No. 51, pp. 25-35, Oct.-Dec., 1986, University of Pennsylvania

[6] G. Dubost, Flat Radiating Dipoles and Applications to Arrays, John Wiley & Sons, Research Studies Press, 1981, pp. 24-28, 66, 18.

[7] H. Jasik, Antenna Engineering Handbook, McGraw-Hill, 1961, Section 3.3.

[8] James, Hall and Wood, Microstrip Antenna Theory and Design, Peter Peregrinus Press Ltd., 1981, pp. 91, 266, 268.

[9] S. Uda and Y. Mushiake, Yagi-Uda Antenna: Sendai, Japan: Sasaki, 1954.

[10] H. Jasik, Ed., Antenna Engineering Handbook, New York: McGraw-Hill, 1961, pp. 3.13-15.

[11] R.W. Lampe, Design Formulas for an Asymmetric Coplanar Strip Folded Dipole, AP-S Transactions, AP-33, No. 9, September 1985, pp. 1028-1031.

[12] Bahl and Bhartia, Microstrip Antennas, Artech Books, 1980, pp. 64-65.

[13] E.A. Wolff, Antenna Analysis, Wiley & Sons, New York, 1966, pp. 262, 295.

[14] I.J. Bahl and P. Bhartia, Microstrip Antennas, Artech House, Dedham, Massachusetts, 1980, pp. 56-63 and p. 50.

[15] J.R. James, P.S. Hall and C. Wood, Microstrip Antenna Theory and Design, Peter Peregrinus Ltd. for IEE, 1981, p. 61.

3.0 OVERALL STUDY CONCLUSIONS

Two microstrip antenna types were analyzed and reduced to practical designs in this study: the microstrip slot antenna and the dual folded dipole (DFD).

The microstrip slot antenna exhibits wide (40%) impedance bandwidth with demonstrated antenna radiation bandwidths of at least 10% frequency spread to -3 dB gain levels. Its low (20%) efficiency, an inherent property of the slot radiator, limits its usefulness to serial arrays of > 10 elements to achieve a useful (> 80%) overall antenna efficiency. Microstrip slot serial array designs are useful for applications like unsteered and shaped beam antenna. They also share the disadvantages of all serial arrays: a narrowing bandwidth as the element number increases and a steering of the main beam with frequency.

Microstrip slot serial array designs with medium bandwidth are possible using the techniques of Solbach [4, Section 1] with the modifications outlined in this report by Prof. Kisliuk. Kisliuk's work improved on Solbach's approach by introduction of the effect of capacity coupling across the microstrip slot. Added work characterizing the susceptance vs. slot dimensions is needed to use this work in low-sidelobe serial array designs.

Analyses of surface wave radiation and microstrip radiation detailed in Section 1 are useful for other microstrip antenna designs seeking to control these radiations in low sidelobe antennas.

The microstrip dual folded dipole (DFD) is especially adaptable for use with MMIC modules when one of its two layers is GaAs and because of its non-contacting coupling between feed and antenna layers. Its high gain of + 7.3 dBi and analytically demonstrated bandwidth of 10% make it useful for large phased array work.

Utility of the DFD design would be improved with added analytic and experimental studies of the trade offs in layer thickness and ϵ vs. antenna gain and bandwidth. The effect of adding a high ϵ superstrate, shown by Alexopoulos, Engheta and others to enhance antenna gain without a large increase in mutual coupling, is an exciting new analysis area that can have an impact on microstrip antennas and merits further exploration.
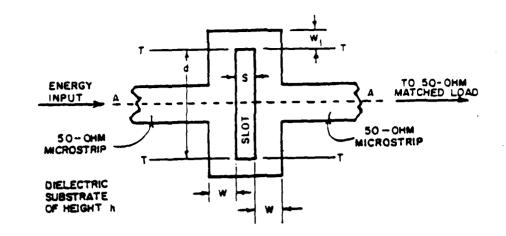
FIGURE 1.1 MICROSTRIP-FED RADIATING SLOT (UPPER VIEW).
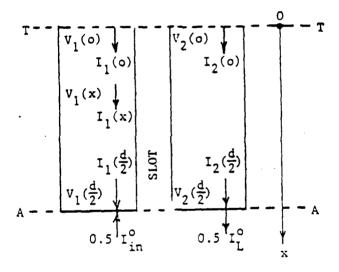
FIGURE 1.2 COUPLED MICROSTRIP LINES MODELING HALF OF THE SLOT.
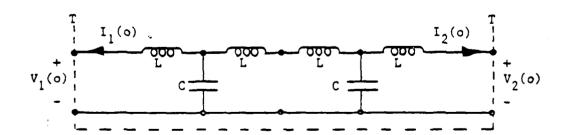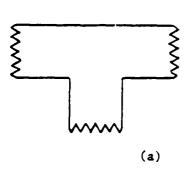
FIGURE 1.3 EQUIVALENT CIRCUIT OF TWO RIGHT-ANGLE BENDS
AT THE END OF THE SLOT.

-63-
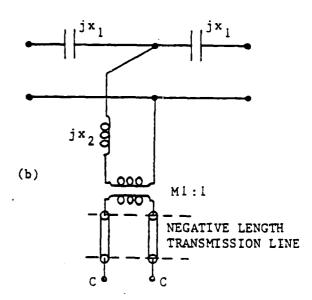
FIGURE 1.4 (a)   TEE JUNCTION   (b) EQUIVALENT MODELLING CIRCUIT
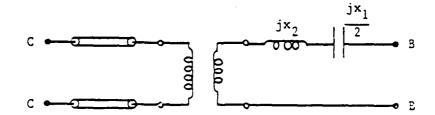
FIGURE 1.5   EQUIVALENT CIRCUIT OF THE T-JUNCTION AT THE
INPUT AND OUTPUT OF THE RADIATING SLOT
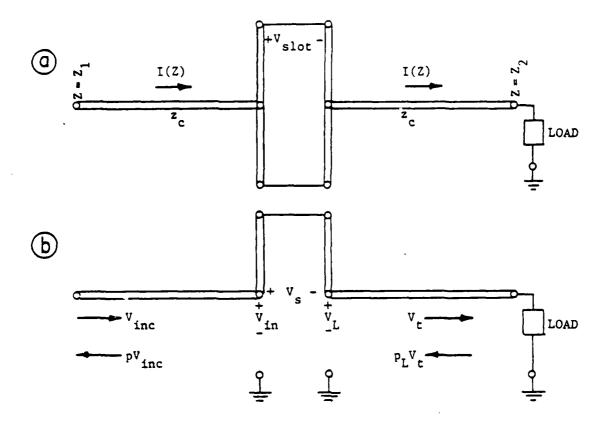
FIGURE 1.6   SIMPLIFIED EQUIVALENT CIRCUIT OF A MICROSTRIP
MEANDER-LINE SLOT ANTENNA

    a. With full meander line
    b. With folded meander line
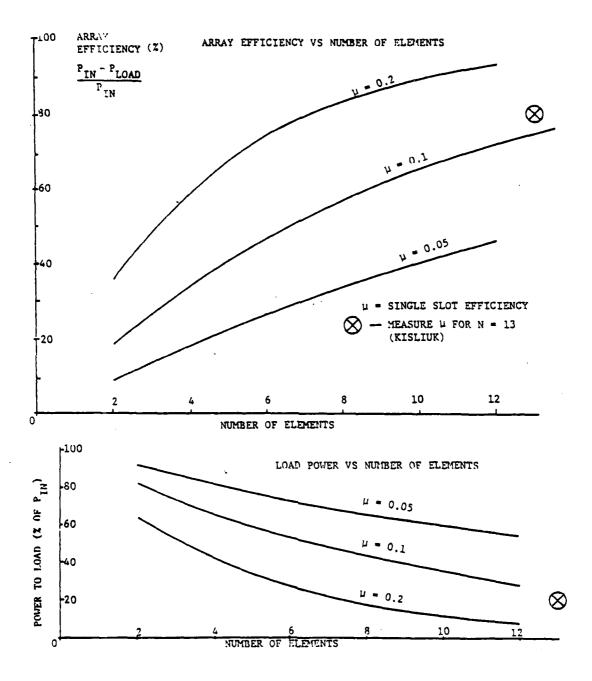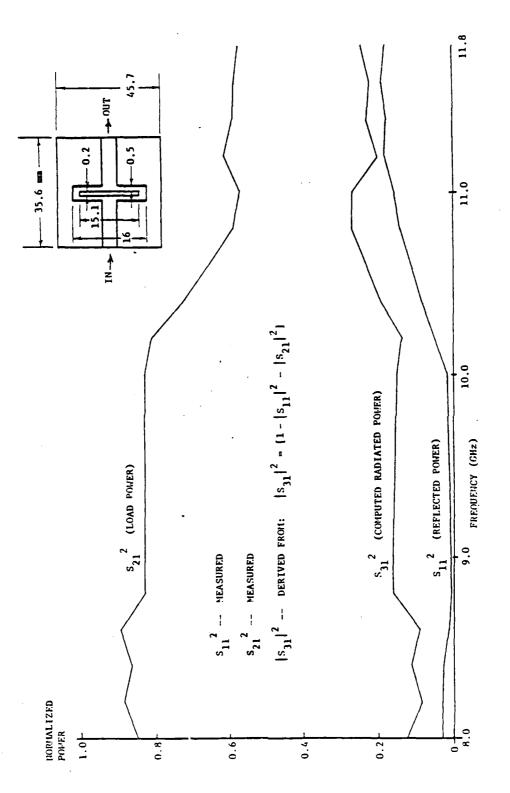
FIGURE 1.7 ARRAY POWER RELATIONS

FIGURE 1.8 POWER RELATIONS: X-BAND MICROSTRIP SLOT ANTENNA
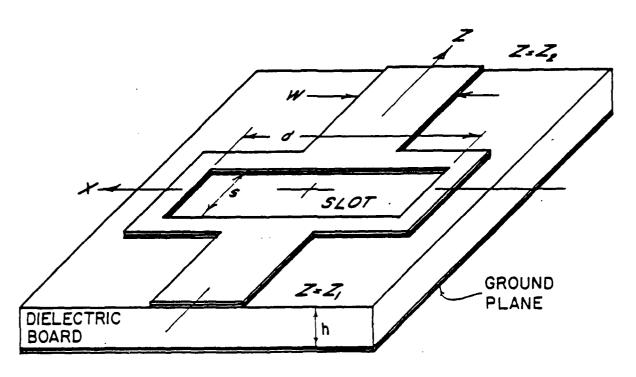
FIGURE 1.9   THE MICROSTRIP SLOT ANTENNA.
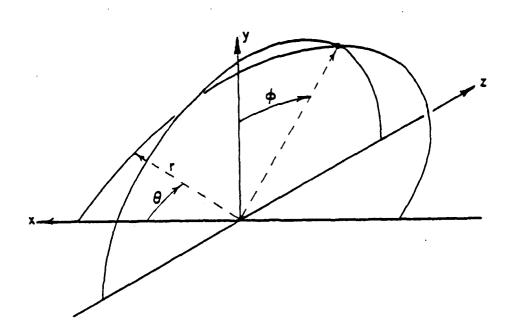
FIGURE 1.10   SPHERICAL COORDINATES IN THE FAR-FIELD ZONE
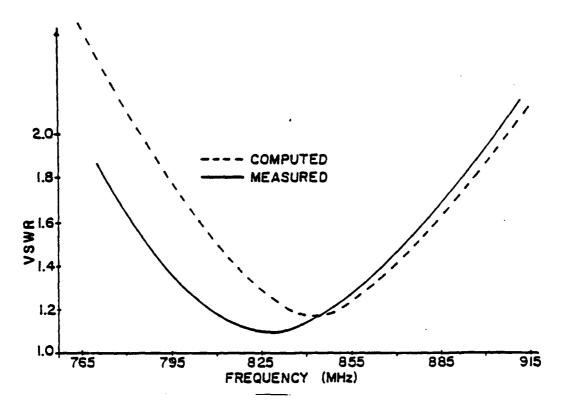
FIGURE 1.11   SINGLE VHF SLOT
DIMENSIONS (in mm):   h=3, d=120.5, W = W1 =15, S=1; ε_r=2.55.
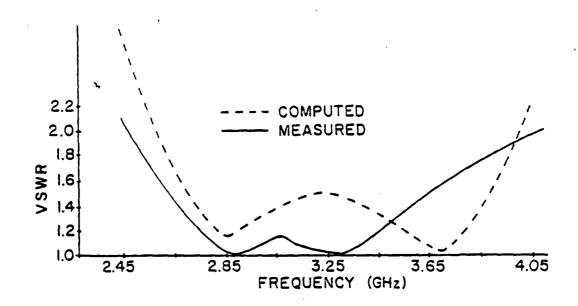
FIGURE 1.12   SINGLE S-BAND SLOT
DIMENSIONS (in mm):   h=3, d=40, W = W1 = 4.7, S=0.2; ε_r=2.55.
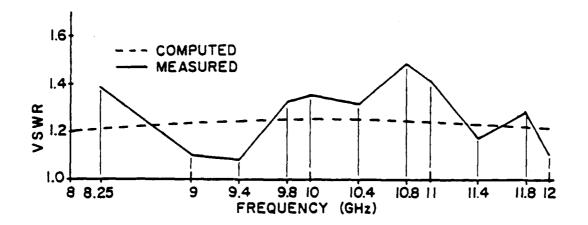
FIGURE 1.13 SINGLE X-BAND SLOT, COMPUTED AND MEASURED.
DIMENSIONS (in mm): h=0.79, d=12.1, W=0.45, W1=0.98, S=0.1, ϵ_r=2.2.
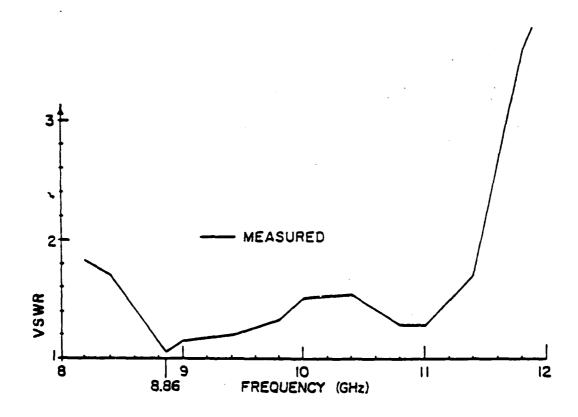
FIGURE 1.14 SINGLE X-BAND SLOT
DIMENSIONS (in mm): h=0.79, d=12.1, W=2.99, W1=3.05, S=0.1; ϵ_r=2.2.
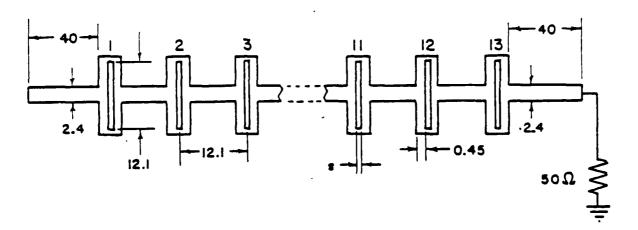
FIGURE 1.15   13-SLOT ARRAY.   THE WIDTH OF THE SLOTS IS TAPERED.
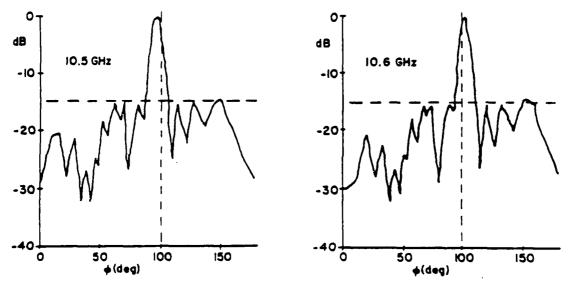
FIGURE 1.16   E-PLANE RADIATION PATTERNS OF THE SLOT ARRAY SHOWN IN
FIGURE 1.15.
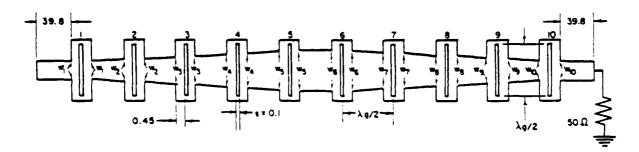
FIGURE 1.17   10-SLOT ARRAY.   THE WIDTH OF MICROSTRIP LINES
FEEDING THE SLOTS IS TAPERED.
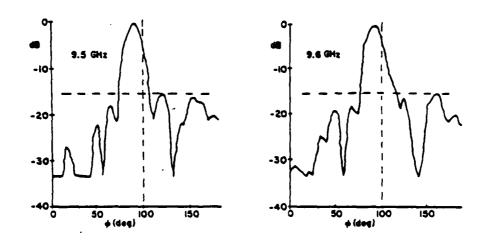
FIGURE 1.18 E-PLANE RADIATION PATTERNS OF THE 10-SLOT ARRAY OF FIGURE 1.17.
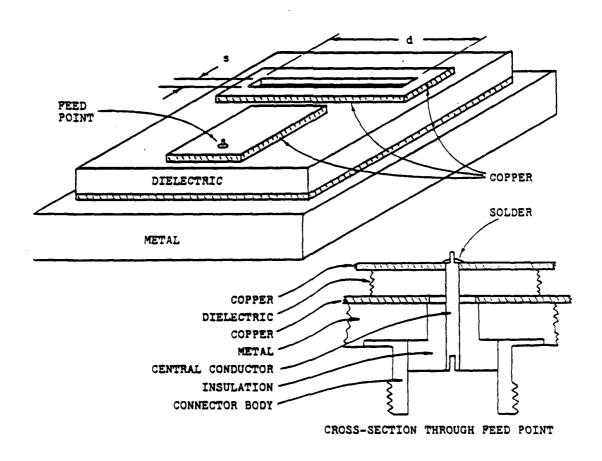
FIGURE 1.19 3-D SKETCH OF A MICROSLOT SHUNT RADIATOR.

PATTERN No.15   DATE: 2/20/86

HIGH EFFICIENCY CONFORMAL ELEMENT
CAPACITY-COUPLED SLOT, 0.5 x 10.9mm
2-SCREW CONNECTOR IN 1/8" PLATE
0.085" DIELECTRIC DIAMETER
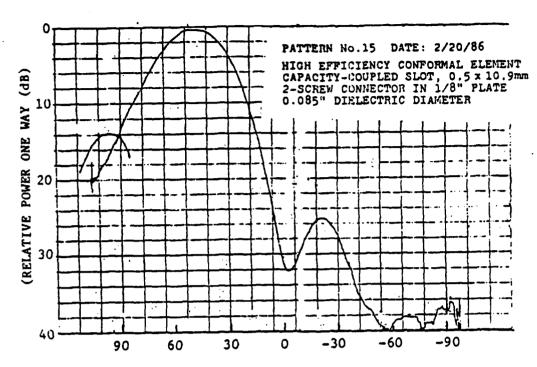
FIGURE 1.20   MICROSLOT SHUNT RADIATOR: PATTERN WITH COAXIAL
EDGE-BOARD FEED.

PATTERN No.19   DATE 2/21/86

CONFORMAL ELEMENT
0.5 × 10.9 SLOT
REAR FEED
E PLANE   f = 8526.5 MHz
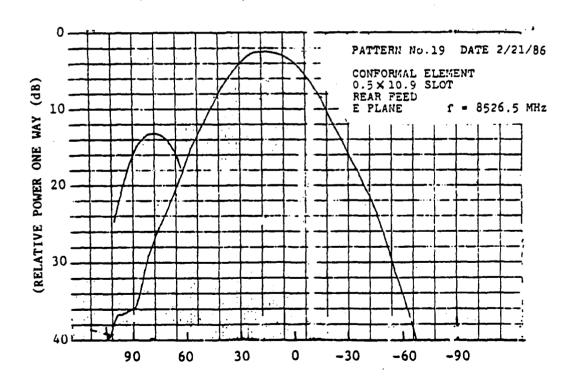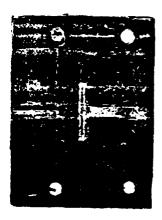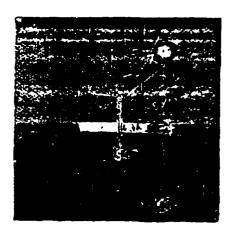
FIGURE 1.21   MICROSLOT SHUNT RADIATOR: PATTERN   WITH COAXIAL REAR-FEED
THROUGH GROUND PLANE.

FIGURE 1.22   PHOTO OF VEE SLOT, 0.5 MM AND 0.2 MM MICROSLOT RADIATORS
USED IN ANTENNA GAIN   STUDIES.

PATTERN No.23   DATE: 2/24/'86

0.2 x 13.06 mm SLOT
CAPACITY-COUPLED   REAR FEED
E PLANE   f = 9154 MHz
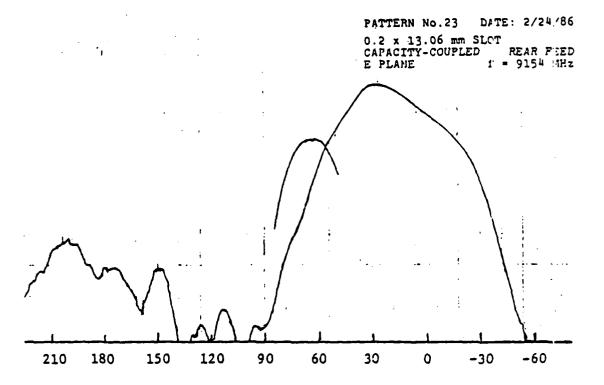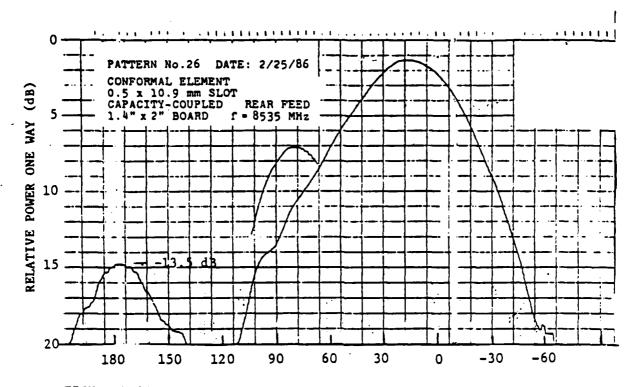
FIGURE 1.23   PATTERN OF 0.2 x 13.2 MM MICROSLOT ANTENNA MEASURED AT
9.154 GHz.   MEASURED GAIN IS - 1.5 dB BELOW THAT OF A
DIPOLE RADIATOR (-1.5 DBD).

FIGURE 1.24   PATTERN OF 0.5 X 10.9 MM MICROSLOT ANTENNA MEASURED AT
8.535 GHz.   MEASURED ANTENNA GAIN IS +0.8 dBd.
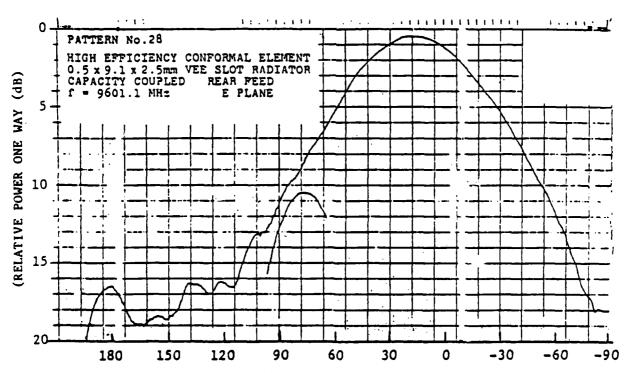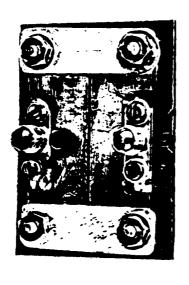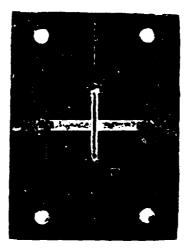
FIGURE 1.25   PATTERN OF 0.5 MM VEE SLOT ANTENNA SHOWN IN FIGURE 1.22
AT 9.607 GHz.   MEASURED ANTENNA GAIN IS 5 dB.

FIGURE 1.26   FRONT AND REAR VIEW OF 0.2 X 12.6 MM SERIAL MICROSTRIP SLOT
TEST BOARD
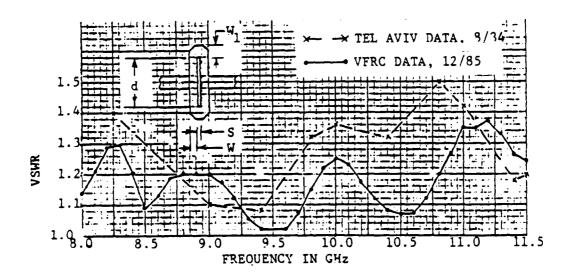
FIGURE 1.27   COMPARISON OF SINGLE X-BAND SLOT VSWR MEASUREMENTS AT
TEL-AVIV UNIVERSITY AND AT VFRC.   DIMENSIONS (in mm):
d = 12.1, w = .45, w_1 = .90, S = .1, h = .79, ϵ_r = 2.2.
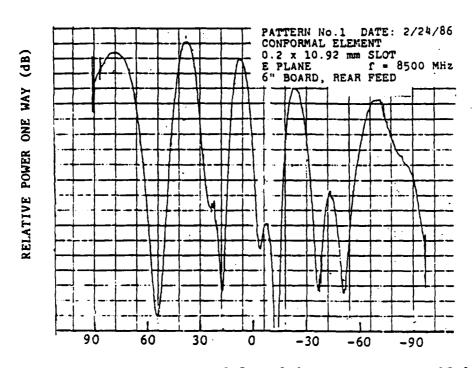
FIGURE 1.28 ANTENNA PATTERN OF 0.5 X 12.6 MM MICROSLOT ON 15.3 CM
DIELECTRIC SUBSTRATE. ε_r = 2.2, CONNECTORS BEHIND
GROUND PLANE.
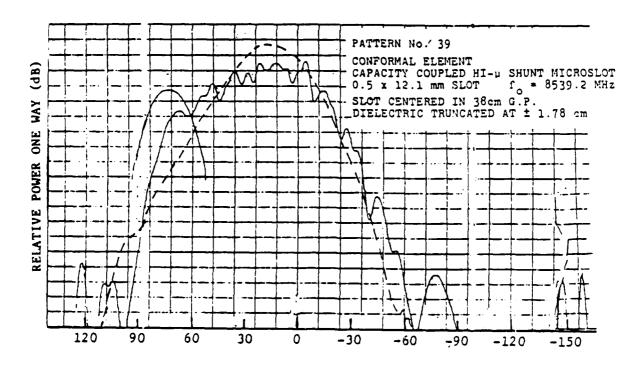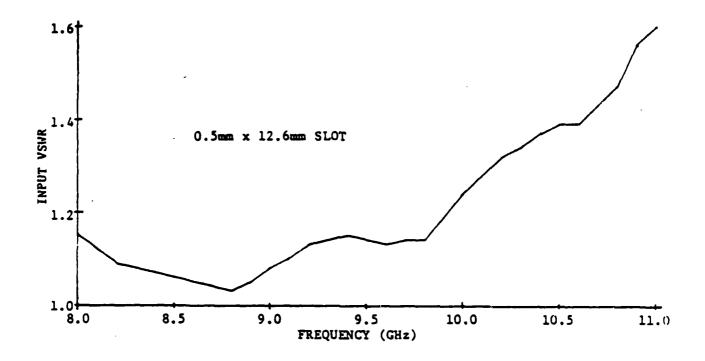
FIGURE 1.29 ANTENNA PATTERN: COMPARISON OF PATTERNS OF 0.5 X 12.6 MM
SLOT RADIATOR WITH (SOLID LINE) AND WITHOUT 38 CM X 20 CM
GROUND PLANE.

FIGURE 1.30   VSWR OF 0.5 X 12.6 MM SLOT RADIATOR USED IN PATTERN TESTS
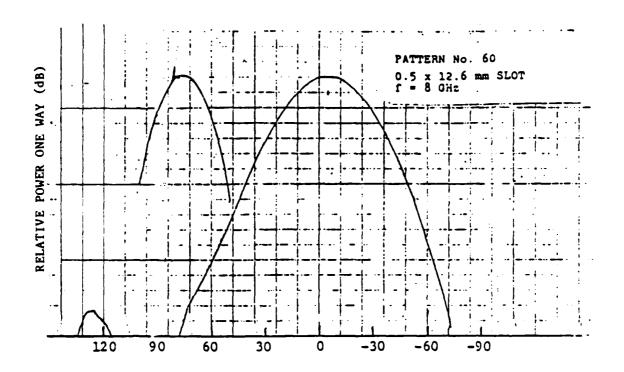
FIGURE 1.31   ANTENNA PATTERN: 0.5 X 12.6 MM SLOT AT 8.0 GHz
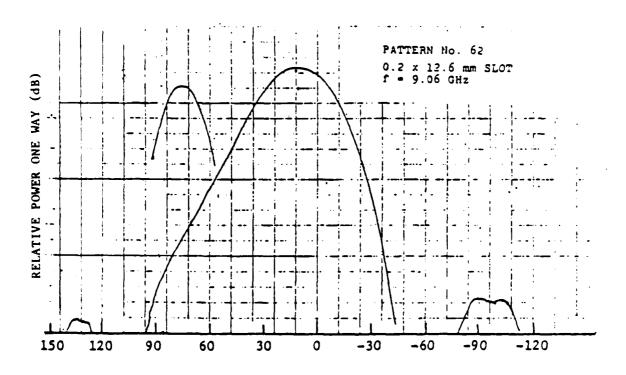
FIGURE 1.32   ANTENNA PATTERN: 0.5 X 12.6 MM SLOT AT 9.0 GHz
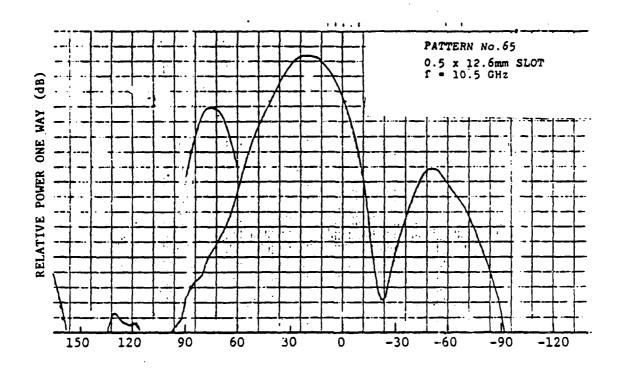
FIGURE 1.33 ANTENNA PATTERN: 0.5 X 12.6 MM SLOT AT 10.5 GHz.
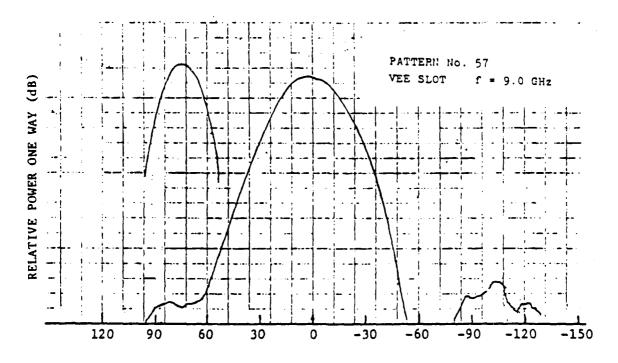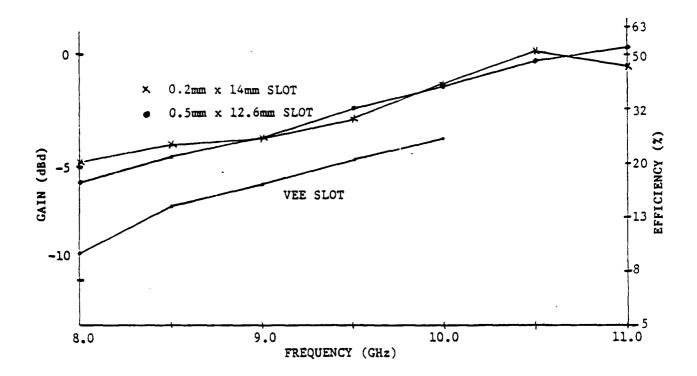
FIGURE 1.34 ANTENNA PATTERN: 0.5 MM VEE SLOT ANTENNA AT 9.0 GHz.
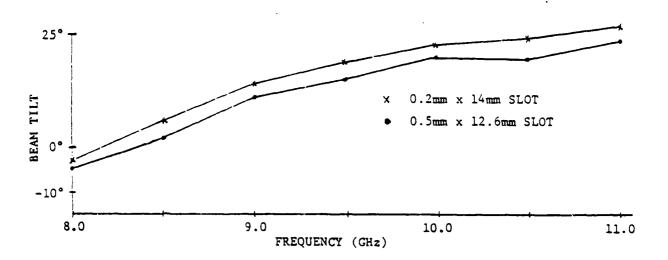
FIGURE 1.35   GAIN AND BEAM TILT VS FREQUENCY GRAPHS FOR 0.5 X 12.6 MM AND
0.2 X 14 MM MICROSTRIP SLOTS AND 0.5 MM VEE SLOT RADIATORS.

PROJECT: CONFORMAL ELEMENT

REMARKS: 0.2 x 14mm SLOT IN
MICROSTRIP LINE

(a) SLOT IN 50-OHM LINE.

(b)(a) PLUS TWO 1.5 x 6mm TABS ON
LINE SPACED ± 63mm.

(c)(b) WITH 42-OHM LINE
BETWEEN TABS.
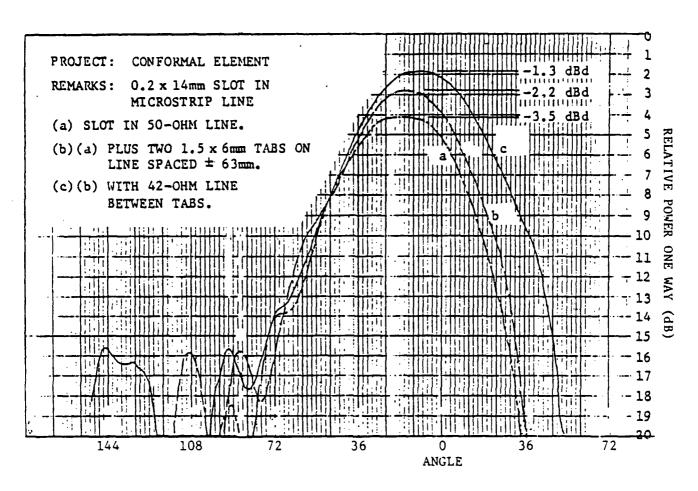
FIGURE 1.36   COMPARISON OF ANTENNA PATTERNS OF
THREE MICROSTRIP SLOT RADIATORS.
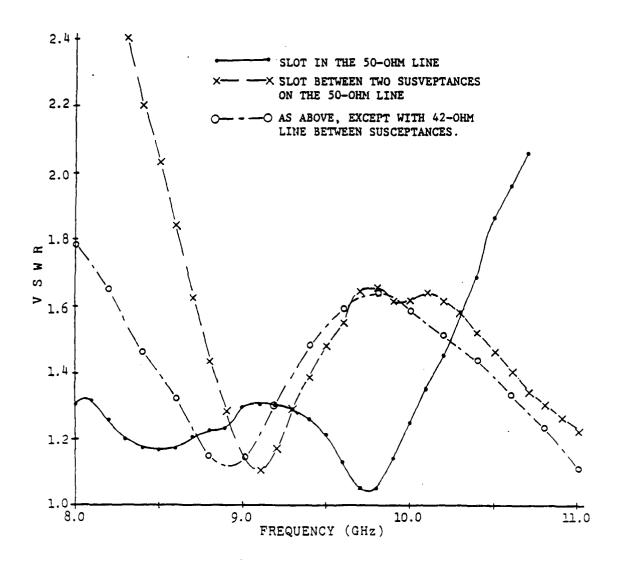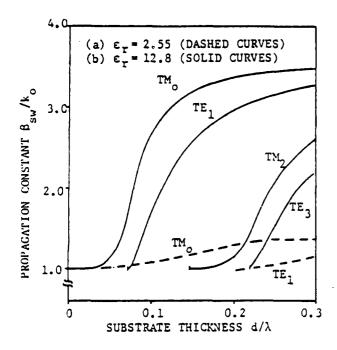
FIGURE 1.37   COMPARISON OF VSWR FOR THREE MICROSTRIP SLOT RADIATORS.

FIGURE 2.1*   NORMALIZED SURFACE WAVE
PROPAGATION FOR A GROUNDED DIELECTRIC
SUBSTRATE: (a) $\epsilon_r = 2.55$. (b) $\epsilon_r = 12.8$

*After Pozar and Schaubert, IEEE Trans.
Antennas & Prop., Vol AP-32, June 1984.
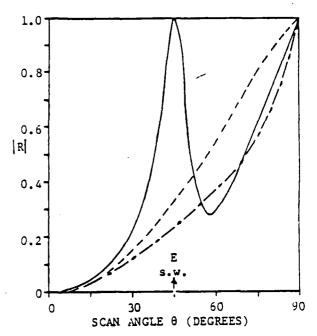
FIGURE 2.2   SCAN CHARACTERISTICS OF
AN INFINITE PRINTED DIPOLE ARRAY.

$a = b = 0.5\lambda$; $L = 0.39\lambda$; $d = 0.19\lambda$.
$w = 0.002\lambda$; $\epsilon = 2.55$.
E-PLANE———; H-PLANE– – –; D-PLANE—– –

Folded Dipole
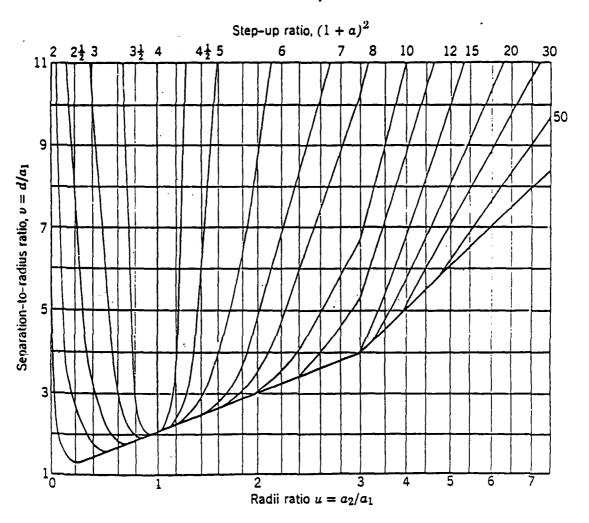
FIGURE 2.3   IMPEDANCE STEP-UP RATIO OF FOLDED DIPOLE.
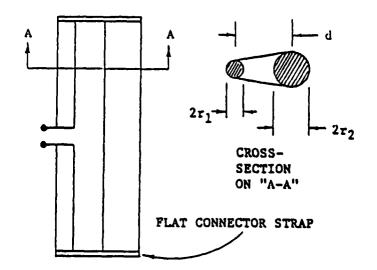
FIGURE 2.4a   PARAMETERS OF ROUND-CONDUCTOR FOLDED DIPOLE.
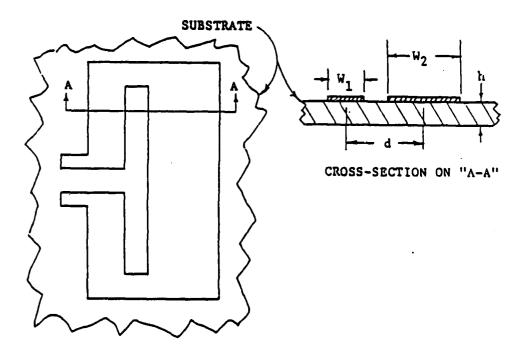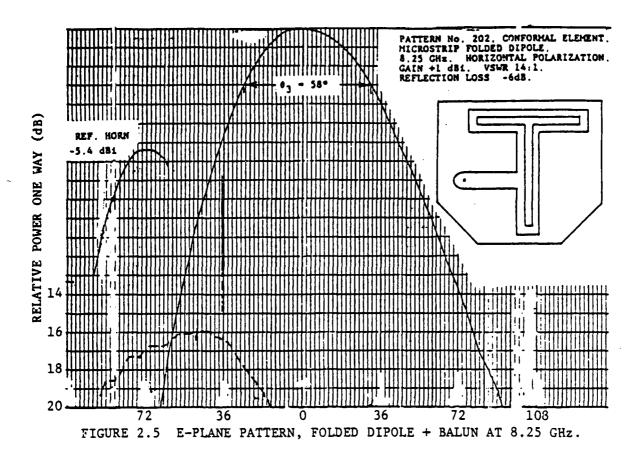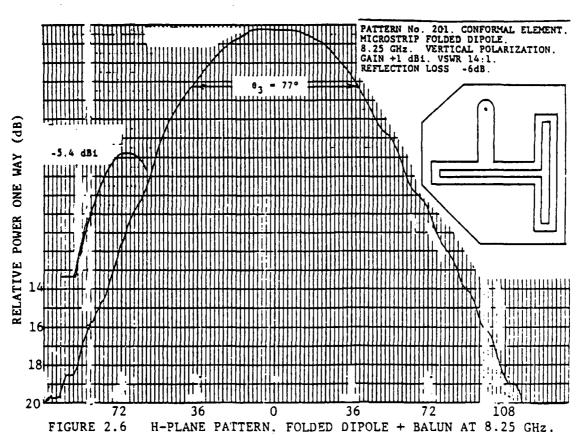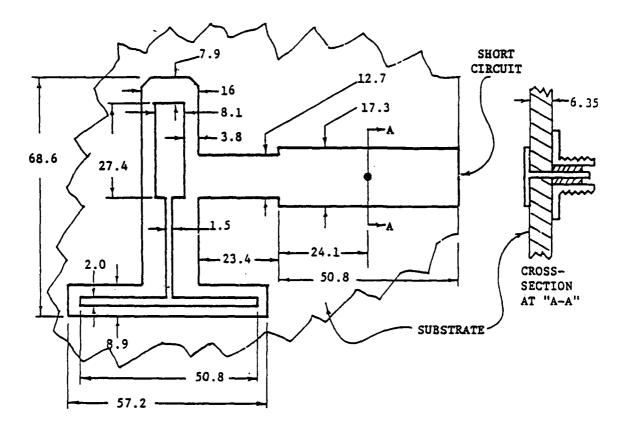
FIGURE 2.4b   PARAMETERS OF MICROSTRIP FOLDED DIPOLE.

PATTERN No. 202. CONFORMAL ELEMENT.
MICROSTRIP FOLDED DIPOLE.
8.25 GHz. HORIZONTAL POLARIZATION.
GAIN +1 dBi. VSWR 14:1.
REFLECTION LOSS -6dB.

FIGURE 2.5   E-PLANE PATTERN, FOLDED DIPOLE + BALUN AT 8.25 GHz.

PATTERN No. 201. CONFORMAL ELEMENT.
MICROSTRIP FOLDED DIPOLE.
8.25 GHz. VERTICAL POLARIZATION.
GAIN +1 dBi. VSWR 14:1.
REFLECTION LOSS -6dB.

FIGURE 2.6   H-PLANE PATTERN, FOLDED DIPOLE + BALUN AT 8.25 GHz.

-87-

FIGURE 2.7   LAYOUT OF S-BAND FOLDED DIPOLE AT 2.25 GHz.
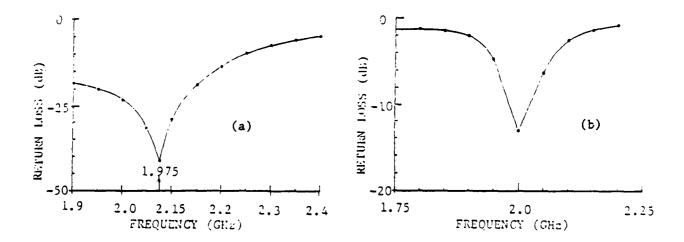
FIGURE 2.8   PREDICTED PERFORMANCE (a), AND MEASURED PERFORMANCE (b),
OF S-BAND BALUN AND FOLDED DIPOLE.
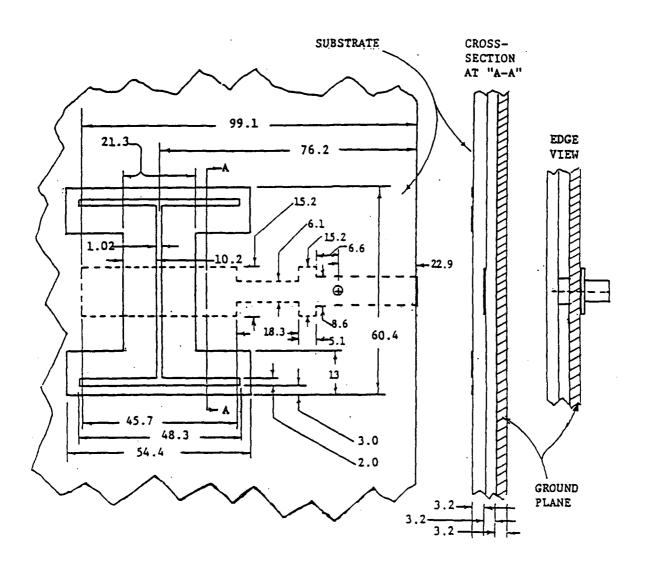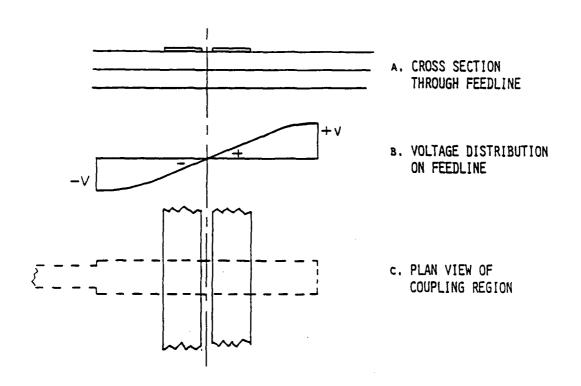
FIGURE 2.9 MICROSTRIP DFD WITH REVISED INPUT CIRCUIT.

A. CROSS SECTION THROUGH FEEDLINE

B. VOLTAGE DISTRIBUTION ON FEEDLINE

c. PLAN VIEW OF COUPLING REGION

FIGURE 2.10   TRANSFORMER COUPLING

| MLSC 50Ω 89.6° | MLIN 50Ω 26° | MSTEP 50/34 | MLIN 34Ω 22.5° | MSTEP 34/60 | MLIN 60Ω 71° | MSTEP 60/34 | MLIN 34Ω 90° | MLIN 20.5Ω 94° | DIPOLE DATA FILE |

50Ω INPUT

ELEMENT CENTERLINE
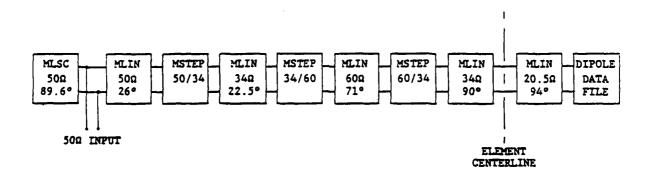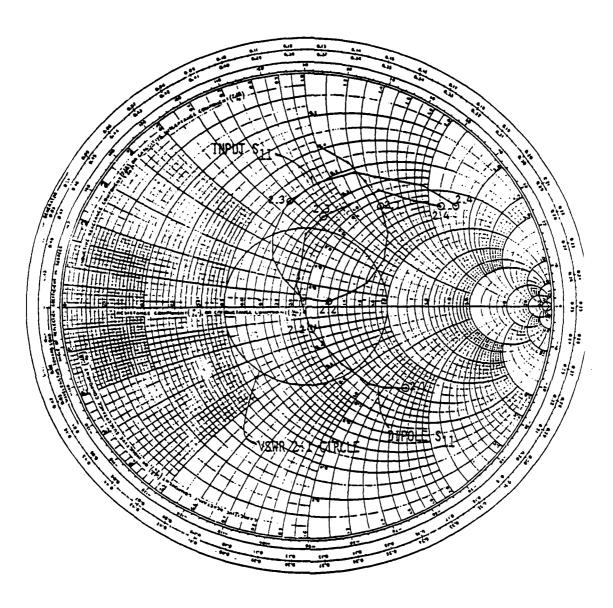
FIGURE 2.11   TOUCHSTONE EQUIVALENT CIRCUIT WITH REVISED INPUT

FIGURE 2.12 ANTENNA AND DIPOLE INPUT IMPEDANCES
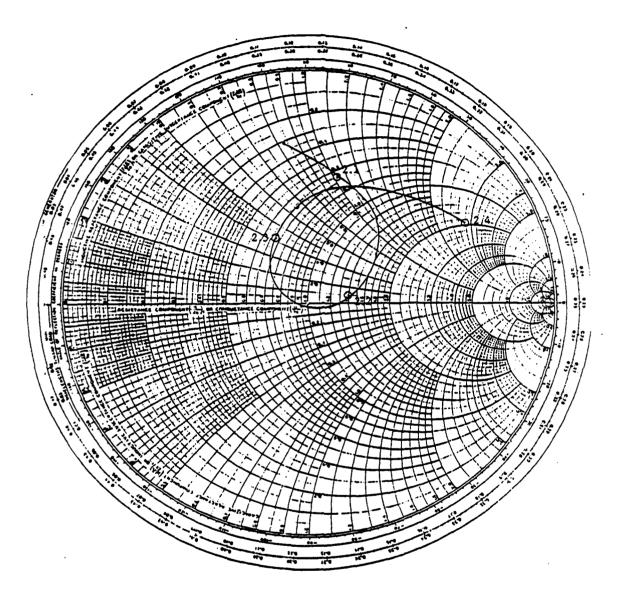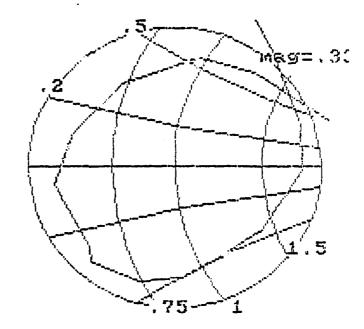
FIGURE 2.13   ANTENNA INPUT IMPEDANCE SYNTHESIZED FROM
              EXPERIMENTAL DATA FILE.

EEsof - 05/20/87 - 14:55:16 - DUFOLD4

⊠ S11
   DUFLD

.5

mag=.30

.2

1: 2.60000

2: 2.40000

1.5

.75   1

FIGURE 2.14 IMPROVED INPUT CIRCUIT IMPEDANCE, 2:1 VSWR CIRCLE.
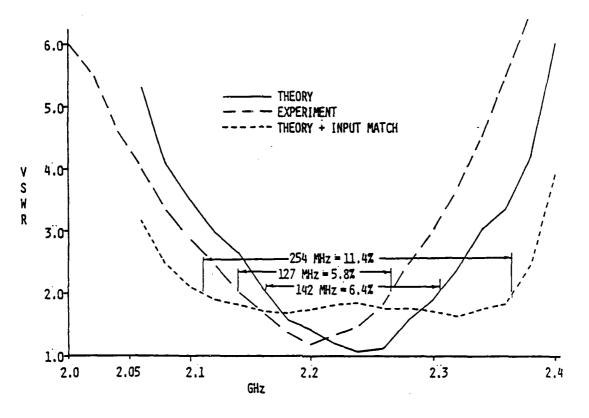
FIGURE 2.15   INPUT VSWR SUMMARY
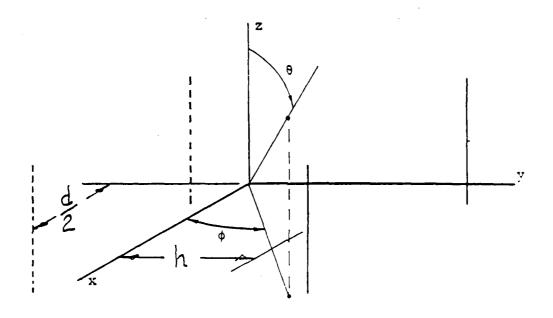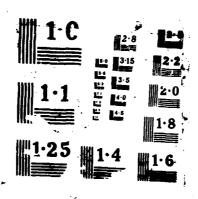
FIGURE 2.16   DUAL FOLDED DIPOLE PATTERN

-94-
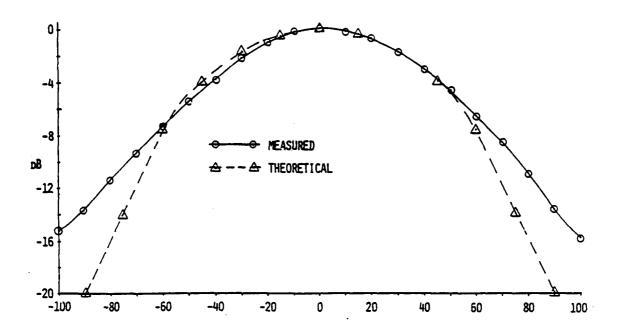
FIGURE 2.17   S-BAND E-PLANE PATTERN OF MICROSTRIP DUAL FOLDED DIPOLE
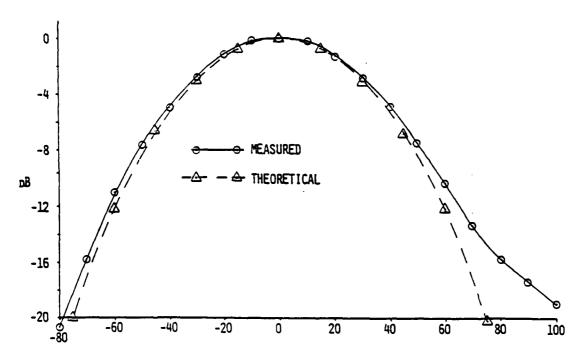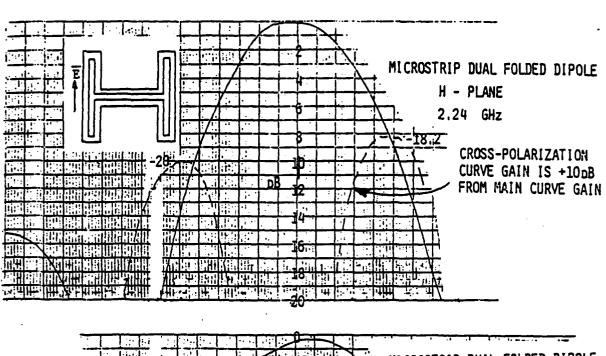
FIGURE 2.18   S-BAND H-PLANE PATTERN OF MICROSTRIP DUAL FOLDED DIPOLE

MICROSTRIP DUAL FOLDED DIPOLE
H - PLANE
2.24 GHz

CROSS-POLARIZATION
CURVE GAIN IS +10dB
FROM MAIN CURVE GAIN

MICROSTRIP DUAL FOLDED DIPOLE
E - PLANE
2.24 GHz

CROSS-POLARIZATION
CURVE GAIN IS +10dB
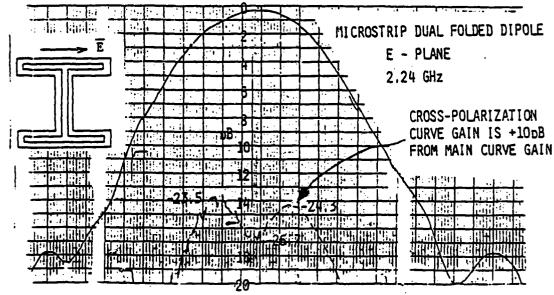FROM MAIN CURVE GAIN

FIGURE 2.19   ANTENNA PATTERNS OF DUAL FOLDED DIPOLE SHOWING
CROSS-POLARIZATION PATTERNS.

-96-

Table 1: Comparison of Microstrip DFD and Patch Antennas
Measured or Calculated at 2.24GHz

Parameter		Dual Folded Dipole (DFD)	Patch
Size		E H .4λ x .46λ	E H .39λE x .45λH
3dB Beamwidth	Theory Measured	78° x 60° 75° x 62°	67° x 76°
Gain		7.4dB measured	7.3dB theory
Bandwidth under 2:1 VSWR		5.5% measured 11% with Input Match	4% theory
Coupling Mechanism:		Transformer Coupling	Direct or aperture Coupling
Mounting Characteristics		Double Dielectric Layer	Single dielectric layer
Adaptability for mm wave circuits		A lower GaAs or Si Layer can mount active Signal processing circuits	Aperture coupling allows mounting S.P. circuits behind ground plane
Active Circuit Area		.5-.6λ square less radiator area in a fully filled array	.5-.6λ square in a fully filled array

MISSION
of
Rome Air Development Center

RADC plans and executes research, development, test and selected acquisition programs in support of Command, Control, Communications and Intelligence (C³I) activities. Technical and engineering support within areas of competence is provided to ESD Program Offices (POs) and other ESD elements to perform effective acquisition of C³I systems. The areas of technical competence include communications, command and control, battle management, information processing, surveillance sensors, intelligence data collection and handling, solid state sciences, electromagnetics, and propagation, and electronic, maintainability, and compatibility.

END

DATE

FILMED

APRIL

1988

DTIC